

Faculté des Sciences
Département de Physique

**Search for a Z' heavy vector boson coupling to
supersymmetric particles in the dilepton and
missing transverse energy final state using the
CMS detector**



Morgane Rigaux

Promotrice: Barbara Clerbaux
Année académique: 2017-2018
Mémoire présenté en vue de l'obtention
du diplôme de Master en Sciences Physiques

Contents

1	Theoretical background	3
1.1	The importance of symmetries	3
1.2	The Standard Model of particles physics and beyond	4
1.3	Grand Unification theories	5
1.4	Supersymmetry	6
1.5	GUT and SUSY inspired models for Z' heavy vector bosons	8
1.5.1	Z' bosons in $U(1)'$ supersymmetric models	8
1.5.2	Leptophobic Z' scenarios in UMSSM models	9
1.6	Mass exclusion limits	11
1.7	Conclusion	12
2	Experimental setup	14
2.1	The Large Hadron Collider (LHC)	14
2.2	Cross section and luminosity	14
2.3	The Compact Muon Solenoid (CMS)	15
2.3.1	General information	15
2.3.2	Detailed detector structure	18
2.3.3	Trigger system	23
2.4	Event reconstruction	24
2.4.1	Particle Flow algorithm	24
2.4.2	Muons	25
2.4.3	Electrons and isolated photons	25
2.4.4	Jets	25
2.4.5	Missing transverse energy	26
3	Data and simulations	27
3.1	CMS 2016 data set	27
3.2	Simulations	27
3.3	Triggers and lepton selection	30
3.4	Reweighting	30
3.4.1	Pile-up reweighting	31
3.4.2	Trigger and reconstruction renormalisation factors	31
4	Implementation of the original selection from [11] and selection optimization	34
4.1	Implementation of the original selection from [11]	34
4.2	Event selection optimization	44
5	Results on the 2016 CMS data and projection for high luminosity	54
5.1	Results on the 2016 CMS data	54
5.2	Projection for high luminosity	59

Abstract

Supersymmetry and Grand Unified Theories are amongst the most popular theories extending the Standard Model of particle physics. A recent paper [11] considers a scenario where a new heavy gauge boson (Z') coupling to supersymmetric particles has a significant production cross section at the LHC and suggests that it could be observed at the LHC in the dilepton and missing transverse energy final state. In this thesis, we study the sensitivity reach of the CMS detector to such a scenario. Using the 2016 LHC data set, corresponding to an integrated luminosity $L = 35.9 \text{ fb}^{-1}$ and a center of mass energy $\sqrt{s} = 13 \text{ TeV}$, an implementation of the dilepton selection proposed in reference [11] is performed and is followed by the design and implementation of a more optimal selection. Expected statistical significances are calculated for the results of both selections, for the 2016 integrated luminosity $L = 35.9 \text{ fb}^{-1}$ and for the integrated luminosity expected for the high luminosity LHC, $L = 3000 \text{ fb}^{-1}$. The results show that the expected significance σ reaches a maximum of $\sigma = 0.04$ at $L = 35.9 \text{ fb}^{-1}$ and $\sigma \sim 0.6$ at $L = 3000 \text{ fb}^{-1}$, hence too small in order to draw conclusions on the validity of the model proposed in [11].

Keywords: high energy physics, Large Hadron Collider (LHC), Compact Muon Solenoid (CMS), heavy vector boson Z' , Grand Unified Theories (GUT), Supersymmetry (SUSY)

Résumé

La supersymétrie et les théories de grande unification (GUT) figurent parmi les théories les plus populaires étendant le Modèle Standard de la physique des particules. Un article récent [11] considère un scénario dans lequel un nouveau boson de jauge massif (Z') possède une section efficace de production significative au LHC et suggère que ce boson pourrait être observé dans l'état final dilepton et énergie transverse manquante. Dans ce mémoire, nous étudions la sensibilité du détecteur CMS à un tel scénario. En utilisant les données récoltées en 2016 au LHC correspondant à une luminosité intégrée $L = 35.9 \text{ fb}^{-1}$ et à une énergie dans le centre de masse $\sqrt{s} = 13 \text{ TeV}$, une implémentation de la sélection des leptons de l'état final proposée dans la référence [11] est effectuée dans un premier temps. Ensuite, une sélection plus optimisée est conçue et également implémentée. La signification statistique attendue est calculée à partir des résultats des deux sélections à la luminosité intégrée de 2016 $L = 35.9 \text{ fb}^{-1}$ ainsi que pour la luminosité intégrée prévue pour le LHC à haute luminosité $L = 3000 \text{ fb}^{-1}$. Les résultats montrent que la signification statistique attendue σ atteint un maximum de $\sigma = 0.04$ à $L = 35.9 \text{ fb}^{-1}$ et $\sigma \sim 0.6$ à $L = 3000 \text{ fb}^{-1}$ et est par conséquent trop faible pour tirer des conclusions concernant la validité du modèle [11].

Mots-clés : physique des hautes énergies, Large Hadron Collider (LHC), Compact Muon Solenoid (CMS), boson de jauge massif Z' , Théories de Grande Unification (GUT), supersymétrie (SUSY)

Remerciements

Je tiens tout d'abord à remercier ma promotrice, Barbara Clerbaux, pour sa disponibilité et pour m'avoir donné l'opportunité de travailler avec elle ces deux dernières années, d'abord dans le cadre d'un stage et puis dans celui de ce mémoire.

Ensuite je tiens particulièrement à remercier Laurent Thomas pour avoir répondu à mes innombrables questions, pour sa disponibilité constante tout au long de ce travail et enfin pour sa relecture attentive. Ce travail n'aurait tout simplement pas pu aboutir sans son aide.

Merci à Laura Lopez Honorez et Ioana Maris pour le temps qu'elles passeront à lire ce mémoire.

Un tout grand merci à Clément Staner, Alexandra Sochnikoff, Matvei Tsishyn et Manon Maisonier pour leur support infailible, en particulier dans mes nombreux moments de doutes et de panique. Merci de ne m'avoir jamais permis de laisser tomber les bras.

Merci également à mes colocataires, pour leur humour et pour m'avoir soutenue pendant la phase de rédaction.

Je remercie bien évidemment mes parents, pour m'avoir permis de faire les études dont je rêvais dans un cadre idéal et pour m'avoir soutenue tout au long de ces années.

Ce mémoire marque la fin de mes années en tant qu'étudiante en physique. Je remercie tous ceux et celles que je ne pourrais nommer explicitement ici mais qui ont égayé mon parcours universitaire et qui m'ont appris beaucoup tant sur le plan intellectuel que sur le plan humain.

Introduction

The twentieth century was marked by the tremendous progress made in our understanding of elementary particles and in particular, the development of the Standard Model (SM), a theory describing three of the four fundamental forces (electromagnetic, strong and weak) as well as all known elementary particles. Its actual formulation was established in the 1970's with the inclusion by Salam and Weinberg of the Brout-Englert-Higgs mechanism into the electroweak interaction originally proposed by Glashow in 1961.

Indeed, any theoretical advancement must be accompanied by the development of technological means in order to design experimental setups to test those theories. In this spirit, dozens of particle accelerators and detectors have been built over the last century, with the underlying idea of being able to reach higher and higher energies in the center of mass of the collision, as it allows to produce particles with higher masses which often characterize particles not contained in ordinary matter. The most powerful accelerator ever built is the Large Hadron Collider, a circular proton-proton accelerator of 27 *km* of circumference located in the neighbourhood of Gevena in Switzerland. The LHC is punctuated by four crossing points for the proton beams corresponding to the localization of the center of four detectors, one of them being the Compact Muon Solenoid (CMS). The LHC is operating since 2008 and has led to several breakthroughs, the most notable being the experimental confirmation of the existence of the Brout-Englert-Higgs boson achieved by the CMS and ATLAS collaborations in 2012, hence almost five decades after its prediction. This discovery marked the closing point of an era in the experimental verification of the SM. The LHC will be upgraded during two years in 2024 and 2025 to the High Luminosity LHC (HL-LHC) which will be operating from 2026 and should accumulate over 3000 fb^{-1} of data over a decade.

Nevertheless, we know that the Standard Model cannot be the end of the story. The reason is twofold; on the one hand the SM is an incomplete theory because, as a non exhaustive list, it fails to provide a candidate for dark matter, to explain the matter-antimatter asymmetry and to account for gravity. On the other hand, it suffers from a lack of internal consistency due to the number of *why's* it leaves unanswered. For example, why are there three families of quarks and leptons ? Why is there such a wide spectrum in the SM particle masses, and also in the strengths of fundamental interactions ? Why does the SM contain 19 free parameters ? All those considerations constitute motivations for expanding the search beyond the MS. The physics beyond the Standard Model (BSM) can consist in extensions of the SM adding other elements such as supersymmetry, e.g. the Minimal Supersymmetric Standard Model (MSSM). But it is also possible to build entirely new theories trying to replicate the results explained by the SM as well as accounting for what the SM fails to elucidate, e.g. string theory.

A recent paper [11] considers a scenario inspired from Grand Unification Theories and Supersymmetry where a new heavy vector boson Z' coupling to supersymmetric particles has a significant production cross section at the LHC. The paper [11] suggests that it could

be observed in final states constituted of two opposite charge leptons and missing transverse energy. In this thesis, we consider three dilepton channels for the final state: dimuon, electron-muon and dielectron channels. In practice, we will first use the 2016 CMS data set in dilepton final states to implement the model of reference [11] and then perform a projection of the result to the expected integrated luminosity of the high luminosity LHC after a decade of running.

The first chapter sets the theoretical background of this work. We begin by introducing the notion of symmetry and its crucial implications in particle physics. Then, the Standard Model (SM) of particle physics is exposed as well as its particle content. By presenting some issues of the SM, we introduce the motivations for the physics beyond the standard model (BSM). We introduce briefly the Grand Unifications Theories (GUT) and supersymmetry (SUSY) and then present GUT and SUSY inspired models for Z' heavy vector bosons, focusing on a particular leptophobic model presented in reference [11].

The experimental setup is reviewed in chapter two. After discussing the general features of the Large Hadron Collider (LHC), we focus on one of the four detectors placed on the LHC: the Compact Muon Solenoid (CMS) and review each detection layer related to our analysis. Finally, the event reconstruction is introduced.

The third chapter covers first the presentation of the 2016 data set and the simulated samples i.e. the backgrounds and signal benchmarks as well as their production cross sections. Then the triggers and other requirement for the leptons are given. Finally, the reweighting procedure performed on the background samples is described.

In the fourth chapter, we implement the selection of the leptons of reference [11] and then propose an alternative selection. The histograms describing each variable entering the selection are presented.

Lastly, we present in the fifth chapter the results of the implementation of the original and alternative selections and show the expected statistical significance for both selections and for both the 2016 integrated luminosity $L = 35.9 \text{ fb}^{-1}$ and the integrated luminosity expected for the High Luminosity LHC $L = 3000 \text{ fb}^{-1}$.

Chapter 1

Theoretical background

To understand the work presented in the following chapters it is necessary to review the basics of the Standard Model of particle physics, defined in section 1.2, and the motivations for its extensions incarnated by the theories beyond the Standard Model. In particular, we will focus on Grand Unified theories (GUT) and supersymmetric (SUSY) extensions of the Standard Model and introduce the Z' bosons as naturally arising from those.

1.1 The importance of symmetries

The concept of symmetry is central to particle physics, hence in this section the notion of symmetry is reviewed, as well as why it is of such importance for particle physics.

A symmetry of a physical system is a property of the system that remains unchanged under some transformation. There are various ways of classifying symmetries, they can either be *continuous* or *discrete*, *local* or *global*, *internal* or *external*.

A square that is rotated around its center will preserve its original appearance only if the angle of the rotation is a multiple of $\frac{\pi}{2}$. This is an example of *discrete* symmetry. On the contrary, a sphere rotated around its axis is an example of *continuous* symmetry, because any angle taken for the rotation will leave the sphere unchanged.

The Noether theorem asserts that to each continuous symmetry corresponds a conserved quantity hence a conservation law. The most obvious examples are time translation that correspond to energy conservation, spatial rotations to angular momentum conservation, and spatial translations to momentum. Therefore, we can point out a first reason for the importance of symmetries, which is they allow to label particles using conserved quantities arising from external and internal continuous symmetries such as the spin, the mass, the charge, the color, etc of a particle [32].

As an additional motivation for what is following, we remind here that quantum field theory (QFT) associates excitations of fields to observable elementary particles.

The transformations of a field acting on spacetime coordinates, e.g. Poincaré and Lorentz transformations correspond to *external* or *spacetime* symmetries [32]:

$$x^\mu \rightarrow x'^\mu(x^\nu)$$

By opposition, transformations acting on the fields themselves correspond to *internal* symmetries and those are of central interest in particle physics [32]:

$$\phi^a(x) \rightarrow M_b^a \phi^b(x)$$

If we take the lagrangian of a scalar field ϕ ,

$$\mathcal{L} = \partial_\mu \phi \partial^\mu \phi^* - V(\phi, \phi^*) \quad (1.1)$$

where ϕ^* denotes the complex conjugate of the scalar field ϕ , then \mathcal{L} is invariant under the transformation:

$$\phi \rightarrow e^{i\alpha} \phi \quad (1.2)$$

where the parameter of the transformation α is a constant. The symmetry of the lagrangian 1.1 under the transformation 1.2 is called a *global* symmetry.

Now, if the parameter of the transformation is taken to be dependent of the spacetime coordinates, $\alpha = \alpha(x)$, the kinetic term in the lagrangian 1.1 is no longer invariant under the transformation 1.2. To restore the invariance of the lagrangian, it is necessary to introduce a new vector field A_μ and to define the covariant derivative D_μ :

$$D_\mu \phi = \partial_\mu \phi + ieA_\mu \phi \quad (1.3)$$

Indeed, performing the replacement $\partial_\mu \rightarrow D_\mu$ into the lagrangian 1.1 allows to recover the invariance under the transformation 1.2 with $\alpha = \alpha(x)$. The symmetry is called a *local* symmetry, the adjective denoting the spacetime dependance of the parameter of the transformation $\alpha(x)$. The procedure to obtain an interacting lagrangian from a free-field lagrangian invariant under some continuous global internal transformation is known as the *gauge principle* [27].

The replacement $\partial_\mu \rightarrow D_\mu$ into 1.1 introduces a coupling between the vector field A_μ and the scalar field ϕ . This last observation illustrates one crucial role of symmetries: they dictate interactions by imposing the couplings via the gauge principle.

1.2 The Standard Model of particles physics and beyond

Unless mentioned otherwise, all information in this section were taken from the reference [17]. The Standard Model (SM) of particle physics is a theory describing the strong, electromagnetic and weak interactions. Each interaction corresponds to the exchange of spin-1 particles amongst the spin-1/2 particles that compose matter. More precisely, the SM is a gauge theory of symmetry gauge group $SU(3)_c \times SU(2)_L \times U(1)_Y$. A gauge theory is a field theory to which is associated a Lie group that contains the set of local transformations leaving the Lagrangian of the considered system invariant.

The particle content of the SM can be split into matter particles: the spin- $\frac{1}{2}$ particles are called fermions and into force carrying particles: the spin-1 particles called gauge bosons. The model also contains a scalar, spin-0 particle, called the Brout-Englert-Higgs boson.

Fermions can be separated into two species depending on their ability to couple to the strong interaction or not. The latter are called leptons, six of them are known today, three are charged and denoted by e, μ, τ and the others are neutral and denoted by ν_e, ν_μ and ν_τ . The former are called quarks, the six of them are charged and denoted by u, d, s, c, b and t . Quarks cannot be found as free particles because of the strength of the strong interaction

and form bound states called hadrons. Each fermion has its corresponding antiparticle, of same mass but opposite charge.

Fermions can be classified into three *generations* or *families* that sorts them by their mass and stability. The first one includes the lightest and most stable particles that compose the world surrounding us. Each generation couples identically to all spin-1 particles.

Hereafter, the gauge bosons associated to each of the three factors of the SM gauge group are introduced. The eight generators G_μ^α with $\alpha = 1, \dots, 8$ corresponding to the $SU_c(3)$ factor are called gluons, they carry a charge of color (hence, the subscript c) and are responsible for the strong interaction. The gauge theory associated is the Quantum Chromodynamics (QCD). The 3 W_μ^a with $a = 1, 2, 3$ are associated with $SU_L(2)$ and the one B_μ to $U_Y(1)$. Together, the four gauge bosons associated to $SU_L(2) \times U_Y(1)$ are related after symmetry breaking to the W^\pm and Z bosons responsible for the weak interaction and the γ photon that mediates the electromagnetic interaction. The particle content of the SM is summarized in the figure 1.1.

The huge success of the SM has been demonstrated by the observation of the W and Z bosons, the gluons, the t and c quarks, all predicted by the SM and more recently, the observation in 2012 at CERN of the scalar boson predicted in the sixties. Still, it cannot account for certain observed phenomena, several examples are listed hereafter:

- The gravitational interaction is not included in the SM. It is natural to search for a theory able to unify gravity with the three other interactions, which would require a formalism including both general relativity and QFT.
- The Big Bang is believed to have produced matter and antimatter in the same amount. Nevertheless, the observable universe is largely dominated by matter. This is referred to as the matter-antimatter or baryonic asymmetry.
- The neutrinos masses implied by neutrino oscillations which have been confirmed by experimentation contradict the prediction of the SM for the neutrinos to be massless.
- The framework of QCD allows the violation of the CP symmetry in the strong interactions, yet no such phenomenon has been observed. This is called the strong CP problem.

These motivate the search for new physics also called physics Beyond the Standard Model (BSM). BSM theories are proposed to explain experimentally observed phenomena that cannot be described by the SM, or deeper explanation of phenomena accounted for by the SM but only with ad-hoc parametrizations [35].

1.3 Grand Unification theories

It is a well established idea that all fundamental interactions may have a common origin, that is, the electromagnetic, weak and strong interactions should be unified at a certain energy [34]. More specifically, it would imply that these three interactions are described by one larger simple gauge group and one unified coupling constant at very high energies. Those theories are called Grand Unified Theories or GUT's and are characterized by an energy scale E_{GUT} above which the unification takes place.

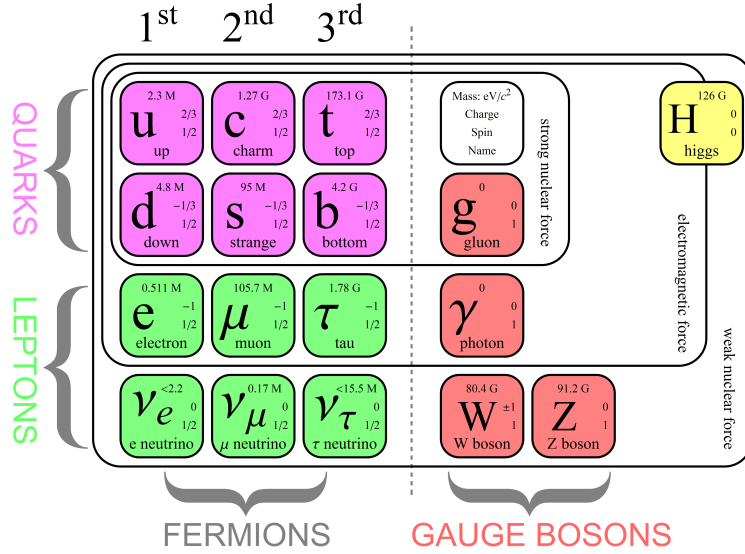


Figure 1.1 – Particle content of the Standard Model of particle physics [8].

A motivation for such theories was given by the success of the electroweak $SU(2) \times U(1)_Y$ model (Glashow, Weinberg, Salam, 1961) in which at high energies $E > E_{weak}$ the electromagnetic and weak interactions are unified into the electroweak interactions while at low energies $E \ll E_{weak}$, only the $U(1)_{em}$ symmetry remains, meaning that the $SU(2) \times U(1)_Y$ symmetry must be broken at a certain energy scale E_{weak} .

The smallest simple gauge group which can contain the SM is given by the $SU(5)$ model (Georgi and Glashow, 1974). LEP and SLC measurements showed back in the nineties that the runnings of the three coupling constants as predicted by this model do not meet in one point at high energy and therefore do not unify [40]. Assuming that GUT's correspond to a physical reality, this observation leads to two possible conclusions, either one ingredient is missing in the model, e.g. supersymmetry, or one should consider GUT's based on larger groups such as $SO(10)$ or E_6 .

The latter always predict the existence of at least one extra neutral gauge boson, denoted by Z' and could break to $G_{SM} \times U(1)'^n$, $n \geq 1$ where $G_{SM} = SU(3) \times SU(2) \times U(1)_Y$ is the SM gauge group [33].

1.4 Supersymmetry

Supersymmetry is a theory introducing a spacetime symmetry between bosons and fermions. In this context, all fermions have a bosonic superpartner of which the spin differs by a half-integer, and vice-versa, meaning that a supersymmetric extension of the SM would comprise at least twice the number of particles of the SM. The operator Q generating a supersymmetric transformation is an anticommutative spinor transforming a bosonic state into a fermionic state and vice-versa [36]:

$$Q|f\rangle = |b\rangle \quad (1.4)$$

$$Q|b\rangle = |f\rangle \quad (1.5)$$

SM fermions	SUSY bosons
leptons	sleptons
quarks	squarks

Table 1.1 – Denomination of the bosonic supersymmetric partners of SM fermions.

SM bosons	SUSY fermions
Z	Zino \tilde{Z}
W^0, W^\pm	Winos $\tilde{W}^0, \tilde{W}^\pm$
gluon g	gluino \tilde{g}
photon γ	photino $\tilde{\gamma}$
Higgs H_u, H_d	Higgsinos \tilde{H}_u, \tilde{H}_d
B^0	bino \tilde{B}^0

Table 1.2 – Denomination of the fermionic supersymmetric partners of the SM bosons.

where $|f\rangle$ denotes a fermion and $|b\rangle$ a boson.

The denomination of the supersymmetric partners of SM particles works as follows: the supersymmetric counterpart of a fermion take the fermion name prefixed by $s-$, as illustrated in table 1.1. For the bosons, their fermionic counterpart are named after the name of the SM boson with the suffixed $-ino$, as shown in table 1.2. Concerning the notation, the supersymmetric particles are topped by a tilde symbol \sim , e.g. the bosonic superpartner of the electron, the selectron, is denoted by \tilde{e} .

Irreducible representations of a supersymmetry algebra corresponding to single-particle states are called *supermultiplets* which contain both boson and fermion states referred to as *superpartners* of each other.

The gauge eigenstates B^0 and W^0 in table 1.2 mix after the electroweak symmetry breaking to give to mass eigenstates Z and γ [36].

The Minimal Supersymmetric Standard Model (MSSM) is an extension of the SM including supersymmetry. It is the minimal SUSY model *"in the sense that it contains the smallest number of new particle states and new interactions consistent with phenomenology"* [14].

The detailed particle content of the MSSM will not be reviewed here but can be found in the reference [36]. We will only specify that supersymmetric bosons can form mixed states.

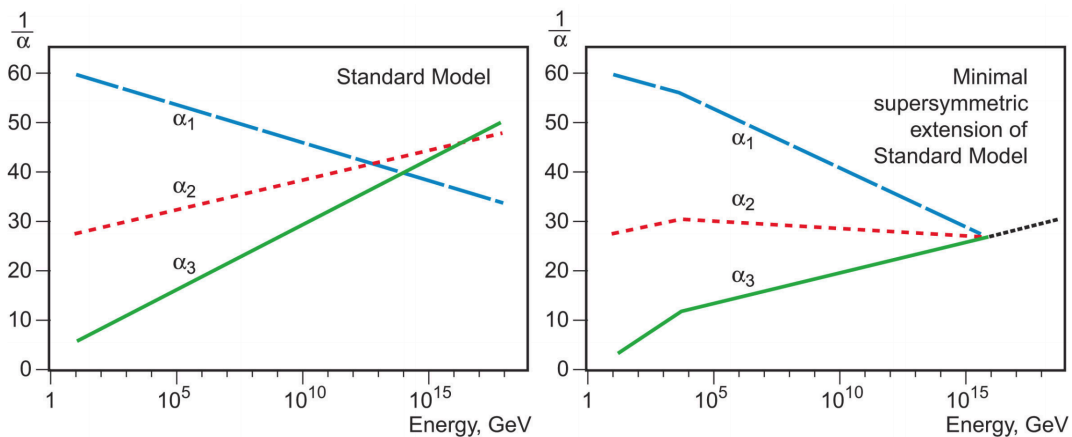


Figure 1.2 – Running of the gauge couplings for $SU(3)_C$ (in green), $SU(2)_L$ (in red) and $U(1)_Y$ (in blue) as a function of energy without (left) and with (right) the MSSM included in the theory [26].

The *neutralinos* are electrically neutral fermions that are mass eigenstates arising from the combinations of higgsinos ($\tilde{H}_d^0, \tilde{H}_u^0$) and neutral gauginos (\tilde{B}, \tilde{W}^0). There are four of them, denoted by $\tilde{\chi}_i^0$ with $i = 1, 2, 3, 4$ and have higher masses with higher index i , hence the $\tilde{\chi}_1^0$ is the lightest neutralino and is usually stable. The *charginos* are two mass eigenstates formed by the combination of charged higgsinos $\tilde{H}_d^-, \tilde{H}_u^+$ and charged winos \tilde{W}^-, \tilde{W}^+ [36].

Including supersymmetry in Grand Unification Theories, e.g. in the form of the MSSM allows to solve several problems encountered by GUTs. For example, it was mentioned in section 1.3 that it is known that GUTs based on a $SU(5)$ group do not achieve a gauge coupling unification at high energy. As illustrated in figure 1.2, this can be solved by including the MSSM in such theory.

1.5 GUT and SUSY inspired models for Z' heavy vector bosons

In this section we briefly review a recent model proposed in reference [11]. We begin by defining the breaking symmetry pattern of the studied model of reference [11]. Then we focus on the leptophobic Z' model proposed in reference [11], we introduce the signal production process and present the two benchmarks investigated in this work.

1.5.1 Z' bosons in $U(1)'$ supersymmetric models

In a GUT based on a E_6 group, a $U(1)'$ symmetry arise from the breaking pattern of E_6 to the electroweak symmetry. Hence, to implement a $U(1)'$ symmetry in a MSSM theory, it is common to use a parametrization inspired by a GUT based on a E_6 group which breaks as follows:

$$E_6 \rightarrow SO(10) \times U(1)'_\psi \rightarrow SU(5) \times U(1)'_\chi \times U(1)'_\psi \rightarrow SU(3)_C \times SU(2)_L \times U(1)_Y \times U(1)'$$

Below E_{GUT} the remaining $U(1)'$ symmetry is a linear combination of $U(1)'_\chi$ and $U(1)'_\psi$ in terms of the E_6 mixing angle θ_{E_6} :

$$Z' = \cos\theta_{E_6} U(1)'_\psi - \sin\theta_{E_6} U(1)'_\chi \quad (1.6)$$

The indices χ and ψ of $U(1)'_\psi$ and $U(1)'_\chi$ denotes different $U(1)'$ models categorized according to the value of the mixing angle θ_{E_6} . The neutral vector bosons associated to $U(1)'_\psi$ and $U(1)'_\chi$ are called Z'_ψ and Z'_χ bosons respectively and a mixing between those two states conforming to equation 1.6 is called a Z' boson.

1.5.2 Leptophobic Z' scenarios in UMSSM models

A Z' scenario is defined as leptophobic when the branching ratio of the Z' into a dilepton pair is around zero:

$$BR(Z' \rightarrow l^+l^-) \sim 0$$

Hereafter, we consider leptophobic Z' scenarios because they present the main advantage of allowing to evade the ATLAS and CMS bounds derived from the dilepton channels that set strong constraints on the possibility of a UMSSM realization, i.e. a MSSM scenario with an additional $U(1)'$ symmetry. The reference [11] shows that in terms of the E_6 mixing angle θ_{E_6} , leptophobic Z' scenarios can be achieved for:

$$-\pi \lesssim \theta_{E_6} \lesssim -\frac{3\pi}{4} \quad (1.7)$$

$$\frac{\pi}{8} \lesssim \theta_{E_6} \lesssim \frac{\pi}{4} \quad (1.8)$$

Different $U(1)'$ symmetries are defined according to different ranges of θ_{E_6} . They are denoted by a greek letter as a subscript, for example equations 1.7 and 1.8 correspond to a $U(1)'_\eta$ symmetry and to the neighbourhood of a $U(1)'_\psi$ symmetry respectively.

We consider dilepton final states originating from a W boson mediated decay of a chargino pair produced by a Z' into charged leptons and missing energy:

$$\tilde{\chi}_1^+ \rightarrow (W^\pm \rightarrow l^\pm \nu_l) \tilde{\chi}_1^0$$

where $\tilde{\chi}_1^+$ and $\tilde{\chi}_1^0$ are the lightest chargino and neutralino respectively. The requirement of a W boson mediated decay of the chargino $\tilde{\chi}_1^+$ into a dilepton pair l^+l^- imposes a minimum mass difference between the chargino $\tilde{\chi}_1^+$ and the neutralino $\tilde{\chi}_1^0$ equal to the mass of the W boson, i.e. $\sim 80 GeV$.

The signal consists in a dilepton pair l^+l^- and missing energy \cancel{E}_T arising from the W mediated decay of a chargino pair $\tilde{\chi}_1^+ \tilde{\chi}_1^-$ produced by a Z' boson itself originating from a proton-proton (pp) collision. The process is shown in figure 1.3.

$$pp \rightarrow Z' \rightarrow \tilde{\chi}_1^+ \tilde{\chi}_1^- \rightarrow l^+l^- + \cancel{E}_T$$

Two signal benchmarks presently not excluded by data are considered, they are denoted respectively by **BMI** and **BMII** and correspond to different $U(1)'$ properties. Both share a common value for the Z' boson mass, $M_{Z'} \sim 2.5 TeV$ and the neutralinos $\tilde{\chi}_1^0$ and charginos $\tilde{\chi}_1^\pm$ are kept as light as possible with the requirement mentioned above of allowing a W boson mediated decay of the chargino pair into the dilepton pair. The values of the E_6 angle θ_{E_6}

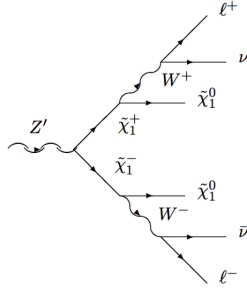


Figure 1.3 – Schematic representation of the production of a dilepton and missing energy final state originating from the W mediated decay of a chargino pair itself induced by a Z' boson [11].

Parameter	θ_{E_6}	$\tan\beta$	μ_{eff} [GeV]	$M_{Z'}$ [TeV]	M_0 [TeV]	M_1 [GeV]
BMI	-0.79π	9.11	218.9	2.5	2.6	106.5
BMII	0.2π	16.08	345.3	2.5	1.9	186.7

Parameter	M_2 [GeV]	M_3 [GeV]	M_4 [GeV]	A_0 [TeV]	A_λ [TeV]	$\sin\chi$
BMI	230.0	3.6	198.9	2	5.9	-0.35
BMII	545.5	5.5	551.7	1.5	5.1	0.33

Table 1.3 – Parameters for the reference points of the two signal benchmarks **BMI** and **BMII**, taken from [11].

for both benchmarks are $\theta_{E_6} = -0.79\pi$ for **BMI** which corresponds to the $U(1)'_\eta$ symmetry and $\theta_{E_6} = 0.2\pi$ for **BMII** which corresponds to the neighbourhood of the $U(1)'_\psi$ symmetry.

The model supposes a coupling unification at the Z' mass scale. The remaining free parameters after some simplifying assumptions have been made (the details of which can be found in reference [11]) are the mixing angle θ_{E_6} , the ratio of the vacuum expectation values of the neutral components of the two Higgs doublet $\tan(\beta) = \frac{v_u}{v_d}$, the effective parameter μ_{eff} ¹, the Z' mass $M_{Z'}$, the common value at the GUT scale for all scalar masses M_0 , gaugino masses M_i with $i = 1, 2, 3, 4$, and trilinear soft couplings A_λ , and the sine of the kinetic mixing angle $\sin\chi$.

The values of the free parameters corresponding to the chosen reference points in the parameter space for the two signal benchmarks **BMI** and **BMII** are listed in table 1.3.

1. Parameter allowing for the resolution of the MSSM- μ problem, see reference [11] p.5 for more details.

The reference [11] proposes a selection for the lepton pairs in the final state, consisting in a set of cuts on different variables to isolate the signal. The backgrounds considered are events with dilepton and missing transverse energy final states originating from $t\bar{t}$, single t , single vector boson (V) or vector boson pairs (VV) possibly with jets. The selection as well as the results of its implementation are shown in table 1.4 for a center of mass energy $\sqrt{s} = 14 TeV$ and an integrated luminosity of $3000 fb^{-1}$. The results are presented in the form of the expected remaining events of background and both signal events from benchmarks **BMI** and **BMII**.

We only mention briefly the different variables entering the selection, as they will be reviewed in details in the next chapters of this work. Jets and leptons candidates have to be such that:

$$\begin{aligned} p_T^l &\geq 20 GeV \text{ and } |\eta^l| < 1.5 \\ p_T^j &\geq 40 GeV \text{ and } |\eta^j| < 2.4 \end{aligned}$$

The first step of the selection summarized in table 1.4 consists in requiring two leptons of opposite charges, N^l being the number of leptons. The reference [11] considers only muon pairs, hence the electron veto. The variable η is called the pseudorapidity and is a spatial coordinate representative of the angle between the direction of a particle and the collider beam, thus the step 3 of the selection is a constraint on the spatial region of the detector for which muons are considered. The next step contains a criteria for the isolation of the muons I_{rel}^μ . Then the variable ΔR is representative of the angular separation of the two muons. After that, a jet veto removes all jet candidates, cuts are applied on the transverse momenta p_t of the leading l_1 and trailing lepton l_2 , defined as the leptons with highest and lowest transverse momentum p_t respectively. The next step consists in implementing a lower bound for the missing transverse energy E_T .

The significance s is defined in reference [11] following:

$$\frac{S}{\sqrt{B + \sigma_B^2}}$$

The significances for the results in table 1.4 are $s = 3.77\sigma$ for the benchmark **BMI** and $s = 7.14\sigma$ for the benchmark **BMII** with $s = \sqrt{s} = 14 TeV$ and $L = 3000 fb^{-1}$.

1.6 Mass exclusion limits

The CMS and ATLAS have so far limited the search for the Z' bosons to SM decay channels. Mass exclusion limits for the Z' have been derived from the study of dilepton and dijet final states.

For dilepton final states, using a combination of $41 fb^{-1}$ and $36 fb^{-1}$ of high-mass dilepton data from pp collisions at $\sqrt{s} = 13 TeV$ collected at the LHC in 2016 and 2017 respectively, the CMS Collaboration sets the mass exclusion limits $M_{Z'} > 4.7 TeV$ for SSM²

2. The Sequential Standard Model (SSM) is an extension of the SM, where the Z' boson has the same couplings to the SM fermions as the Z boson.

Step	Requirement	Background	BMI	BMI
0	Initial	1.7×10^{11}	8.8×10^3	1.9×10^4
1	$N^l = 2$	6.1×10^8	401	860
2	Electron veto	2.9×10^8	100	230
3	$ \eta < 1.5$	1.7×10^8	76	170
4	I_{rel}^μ	7.9×10^5	63	130
5	$\Delta R(l_1, l_2) > 2.5$	7.9×10^5	62	130
6	Jet Veto	7.7×10^4	57	120
7	$p_t(l_1) > 300 \text{ GeV}$	44	36	71
8	$p_t(l_2) > 200 \text{ GeV}$	20	19	32
9	$\cancel{E}_T > 100 \text{ GeV}$	10	14	27

Table 1.4 – Selection of paper [11] for an energy in the center of mass of the collision $\sqrt{s} = 14 \text{ TeV}$ and an integrated luminosity $L = 3000 \text{ fb}^{-1}$.

and $M_{Z'} > 4.1 \text{ TeV}$ for the GUT inspired model Z'_ψ [23]. The ATLAS Collaboration, using 36.1 fb^{-1} of data from pp collisions at $\sqrt{s} = 13 \text{ TeV}$ collected in 2015 and 2016, gets $M_{Z'} > 4.5 \text{ TeV}$ for SSM and $M_{Z'} > 3.8 - 4.1 \text{ TeV}$ in $U(1)'$ models [12].

For dijet final states, the limits are $M_{Z'} > 2.7 \text{ TeV}$ for CMS [22] and $M_{Z'} > 2.1 - 2.9 \text{ TeV}$ for ATLAS. [13].

According to the reference [11], even without considering the leptophobic condition, allowing the opening of supersymmetric decay channels for the Z' boson lowers its mass exclusion limits by a significant factor, up to 200 GeV for dilepton final states and even more for dijet final states.

1.7 Conclusion

The recent model proposed in reference [11] shows that it is promising to consider the inclusion of supersymmetric decay channels for the Z' because it results in a substantial lowering of the actual Z' mass exclusion limit. Moreover, according to the reference [11], if the Z' is chosen to be leptophobic then by applying an appropriate selection on the two well chosen signal benchmarks it is possible to discriminate the signal from the background with a significance between 3σ and 7σ for an integrated luminosity 3000 fb^{-1} which will be reachable with the upgrade of the LHC to the High-Luminosity LHC. Consequently, the

model of reference [11] constitutes a concrete opportunity to discover both a new gauge boson and supersymmetry.

Chapter 2

Experimental setup

2.1 The Large Hadron Collider (LHC)

The Large Hadron Collider is a proton-proton circular collider of 27 km of circumference, part of the accelerator complex of CERN near Geneva, Switzerland. The proton source is a bottle of hydrogen. After creating proton bunches by a process that will not be detailed here, the protons are first accelerated in various machines before being injected in the LHC, as shown in figure 2.1. Two proton beams travel separately and in opposite directions in pipes maintained at super high vacuum at a speed close to the speed of light before colliding in one of the four colliding points corresponding to the central position of the four detectors located on the LHC. Superconducting magnets are disposed along the accelerator, generating a strong magnetic fields that allows to bend the proton trajectories.

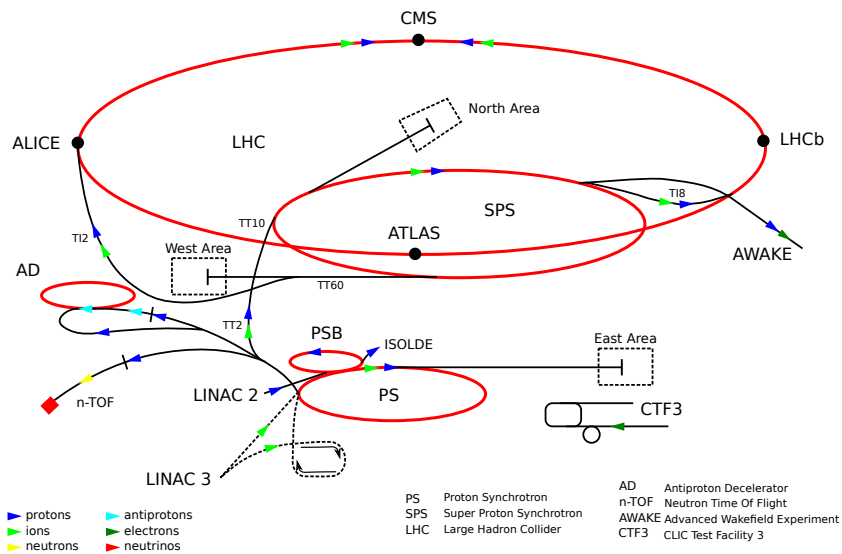


Figure 2.1 – CERN accelerators complex [4].

2.2 Cross section and luminosity

The cross section σ is a quantity measuring the occurrence probability of a given process. It is an intrinsic property of the process and depends on the type of particles interacting as well as on the type of interaction (electromagnetic, strong or weak). The cross section is usually expressed in femtobarns fb , $1fb = 10^{-43} m^2$, or in picobarns pb , $1pb = 10^{-40} m^2$.

The instantaneous luminosity is a measure of the ability of a particle accelerator to produce a certain number of interactions and is the proportionality factor between the number of events per second $\frac{dN}{dt}$ and the interaction cross section σ :

$$\frac{dN}{dt} = \mathcal{L}\sigma$$

\mathcal{L} is therefore expressed in $s^{-1}m^{-2}$. It can be expressed in the following way:

$$\mathcal{L} = \frac{N_b n_b f_{rev} \gamma}{4\pi \epsilon_n \beta^*} F \quad (2.1)$$

in terms of the number of particles per bunch N_b , the number of bunches in the beam n_b , the revolution frequency f_{rev} , the relativistic factor γ , the normalized beam emittance ϵ_n , the beta function at collision point β^* and a luminosity reduction geometrical factor F due to the crossing angle at the intersection point [43].

The F factor accounts for the influence of an angle between the two opposite beams on the luminosity while the normalized emittance is a measure of the dispersion of charged particles in the plane transverse to the beam.

The relation 2.1 indicates that the number of events per second is higher with a larger number of particles per bunch and a larger number of bunches per beam. Moreover, beams that are well aligned and transversally calibrated lead also to a higher instantaneous luminosity.

The integrated luminosity L is defined as the instantaneous luminosity \mathcal{L} integrated over a certain time interval and represents therefore the total number of events by cross section units over a certain time laps. In other words, the higher the integrated luminosity, the larger the quantity of data recorded, which makes it a crucial parameter to determine collider performances.

The figure 2.2 presents the integrated luminosity as a function of time over a one year period, for each of the LHC running year. One can see that the LHC has reached growing energy in the center of mass of the collision over the years, starting with $\sqrt{s} = 7 TeV$ in 2010, then $\sqrt{s} = 8 TeV$ in 2012 and $\sqrt{s} = 13 TeV$ since 2015.

2.3 The Compact Muon Solenoid (CMS)

2.3.1 General information

The Compact Muon Solenoid (CMS) is one of the four detectors located on the LHC. It is a general-purpose detector, which means it is designed to study a broad variety of phenomenas from precise SM measurements to search for new physics that might occur in the LHC. The detector has an cylindrical onion shaped structure made of several detection layers as represented in figure 2.3.

The detector tasks are the followings: to bend the charged particle trajectories, which is accomplished by a solenoid magnet made of superconducting fibers generating a 3.8 Tesla magnetic field; to identify the tracks belonging to a given collision, which is realised by the silicon tracker in the inner center; and finally to measure the energy associated to the products of a collision which is done by the electromagnetic and hadronic calorimeters. A

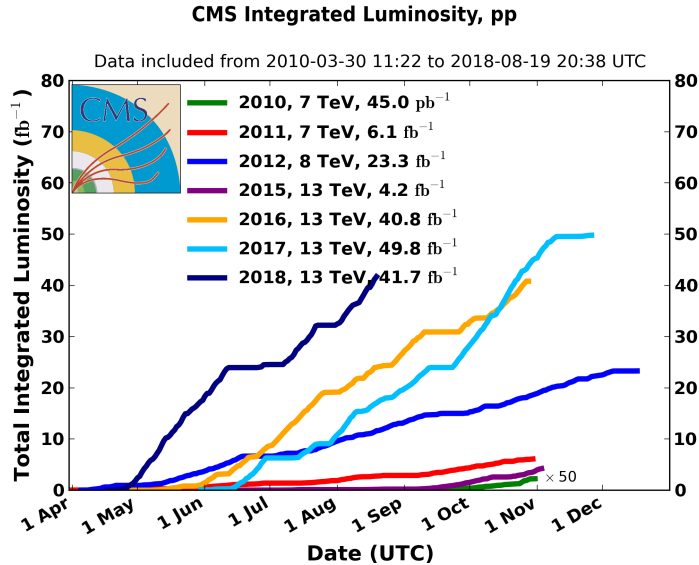


Figure 2.2 – Integrated luminosity as function of time over a one year period, for each of the LHC running year [6].

key feature of the detector is also the good measurement and reconstruction of muons, which are undertaken by the muon system.

In the next section, those main components will be reviewed in more details, from the center of the detector outwards. A particular attention will be drawn on leptons and missing transverse energy, since they constitute the final state of interest in this work.

The coordinate system of CMS is defined such that the origin coincides with the collision point, the x axis is pointing towards the center of the LHC, the y axis is pointing upwards and the z axis is defined accordingly to a right coordinate system and corresponds to the beam axis [1]. The azimuthal angle $\phi \in [0, 2\pi]$ and the polar angle $\theta \in [0, \pi]$ are calculated starting from the x axis and the z axis respectively towards the y axis.

The rapidity y of a particle is defined in terms of the components of its momentum quadrivector $p^\mu = (E, p_x, p_y, p_z)$ by :

$$y = \frac{1}{2} \ln \left(\frac{E + p_z}{E - p_z} \right)$$

and the pseudorapidity η of a particle is defined as

$$\eta = -\ln \left(\tan \left(\frac{\theta}{2} \right) \right)$$

in terms of the angle θ [45].

The rapidity y of a particle of which the mass is negligible, i.e. travelling at a speed close to the speed of light, is equal to the pseudorapidity η of the particle. Besides, the difference of rapidities Δy is invariant under a boost in the z direction. Hence, the pseudorapidity η is often used instead of the angle θ . The pseudorapidity η allows to define two regions of the detector; the barrel corresponding to $0 < |\eta| \lesssim 1.5$ and the two endcap regions corresponding to the $1.5 \lesssim |\eta| \lesssim 3.0$ region. The barrel and endcap regions are separated by the crack region in which the particles are less precisely measured, due to the presence of

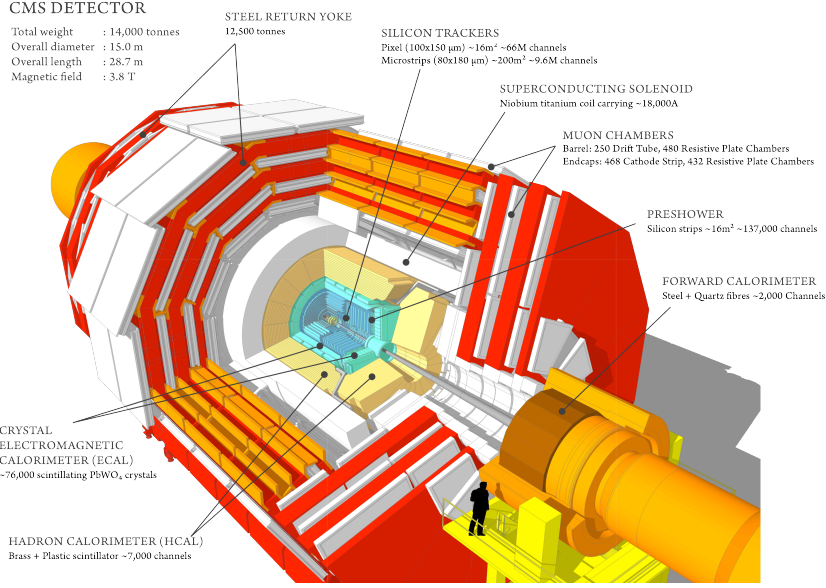


Figure 2.3 – Representation of the CMS detector [3].

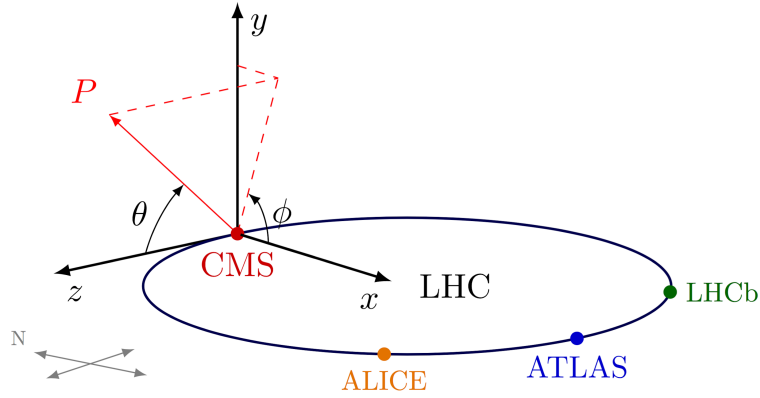


Figure 2.4 – Coordinate system of the CMS detector [7].

cables in this area.

Another important quantity is the transverse momentum p_t , defined as the momentum contained in the transverse plan, i.e. the plan perpendicular to the beam. If $p^\mu = (E, p_x, p_y, p_z)$ is the 4-vector¹ of the momentum of a particle, then:

$$p_t = \sqrt{p_x^2 + p_y^2}$$

1. Here and in the rest of this work, we consider natural units, i.e. $\hbar = c = 1$.

2.3.2 Detailed detector structure

The silicon tracker

The silicon tracker is the closest device to the beam pipe. Its purpose is to measure the direction and the momentum of charged particles by tracking their positions in a set of different points and then fitting the trajectory to the measurement.

A relation between the track curvature and the transverse momentum of a given particle with unitary charge is given by:

$$p_T[\text{GeV}] = 0.3B[\text{T}]R[\text{m}]$$

in terms of the magnetic field B generated by the solenoid magnet and the radius R of the track curvature.

The CMS tracker uses exclusively silicon detectors because it is affordable, it is resistant to radiations and allows a position resolution of the order of $5\ \mu\text{m}$ and a high granularity, both necessary for a good vertex reconstruction. The tracker comes in two parts; the pixel detector makes the core of the three cylindrical layers of silicon pixels and is surrounded by the strip detector composed of layers of silicon strips. The pixel detector is composed of 65 million pixels connected individually to read-out chips, each of them with a size of $100\ \mu\text{m} \times 150\ \mu\text{m}$. The strip detector is made of basic blocks called modules, each of them holding one or two silicon sensors. The basic mechanism is the same for both pixel and strip detectors. A charged particle crossing the sensor loses a really small amount of energy, but sufficient to create thermal excitation that produces electron-holes pairs that can move in the sensor towards the electrodes. The signal is then amplified by the electronics.

The number of layers is a balance between two observations. On the one hand, a large number of layers corresponds to a larger set of points of the trajectory recorded, hence a easier reconstruction. But on the other hand, the multiple scattering process scales with the amount of material crossed, meaning the number of layers should be kept as low as possible.

Figure 2.5 shows a view of the CMS tracker in the r - z plane. Horizontal and vertical lines correspond to barrel and endcaps layers respectively. The red lines represent the pixel detector layers, while black and blue lines denote single and double-sided (or stereo) strip layers respectively. From the center outwards, the strip detector is composed of four inner barrel (TIB) layers and three disks that form the inner endcaps (TED), surrounded by six outer barrel (TOB) layers and two outer endcaps (TEC) each composed by six modules.

The track fitting procedure is based on the Kalman filter, an iterative algorithm that, starting with a rough estimation of the track parameters, improves its estimation of those parameters at each step using the recorded measurements.

The Electromagnetic Calorimeter ECAL

A calorimeter is a block of material aiming at measuring the energy of particles crossing it. It is composed of absorber and active materials. The incident particle initiates a hadronic or electromagnetic shower by interacting strongly or electromagnetically with the absorber. The shower particles have decreasing energy with each step of the shower and are completely absorbed at the end of the process. In the active material, the signal is produced by the

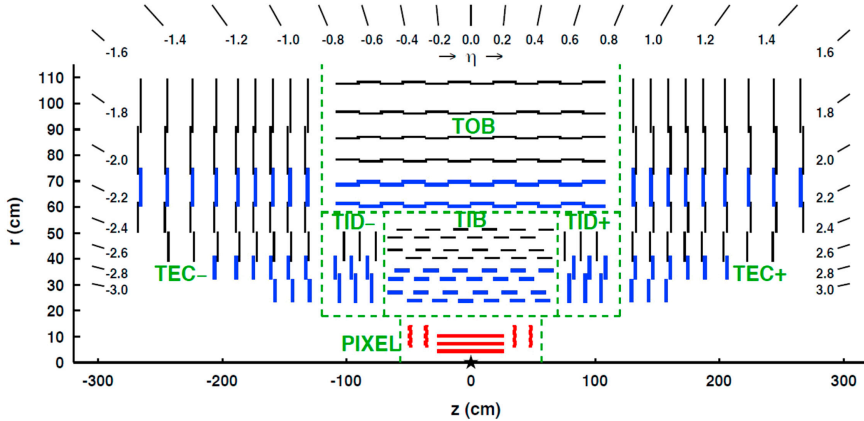


Figure 2.5 – View of the CMS tracker in the r-z plane [42].

energy deposited by charged particles by electromagnetic interaction. It is important to note that calorimetry is a destructive process because particles crossing the calorimeter are completely absorbed.

Calorimeters can be either homogeneous, which means they are composed of only one material playing both roles of absorber and active materials, or sampling, alternating layers of absorber and active materials. The choice of one or the other building technique is a balance between position and energy resolutions. Indeed, in a homogeneous calorimeter, the entire energy of the incoming particle is by definition deposited in the active material, allowing for a good energy resolution. But longitudinal and lateral segmentation are more complicated than in sampling calorimeters, which is a problem when dealing with position measurements [29].

The energy resolution of a calorimeter is the sum of three contributions [43]:

$$\left(\frac{\sigma(E)}{E}\right)^2 = \left(\frac{S}{\sqrt{E}}\right)^2 + \left(\frac{N}{E}\right)^2 + C^2 \quad (2.2)$$

The stochastic term $\frac{S}{\sqrt{E}}$ arises from the stochastic nature of the shower development, causing fluctuations along its expansion. The noise term $\frac{N}{E}$ is caused by electronic noise and pile-up of particles at high luminosity and the constant term C include energy-independent contributions. Therefore, a calorimeter has to be optimized depending on the energy range of the experiment it is built for because the relative importance of the terms in equation 2.2 depends on the energy of the incident particle. The relation 2.2 indicates that the intrinsic energy resolution of a calorimeter improves at higher energies.

The CMS electromagnetic calorimeter (ECAL) is a homogeneous calorimeter composed of 75,848 $PbWO_4$ scintillating crystals arranged in a barrel section (EB) and two endcaps (EE). Together, EB and EE have a coverage in pseudorapidity up to $|\eta| < 3$. The properties of tungstate $PbWO_4$ made it an ideal choice: it has a high density (8.28 g/cm^3) and a short radiation length (0.89 cm) allowing to build a compact calorimeter. Moreover, it has a small Molière radius² (2.2 cm), which concedes the calorimeter a high precision on the shower

2. The Molière radius is a constant of a given material measuring the transverse elongation of an EM shower containing 90% of the initial electron or photon energy.

position.

A charged particle crossing a scintillating crystal induces excitation of the atoms of the crystal, which then deexcites by emitting light. The produced light is then collected by photodetectors: avalanche photodiodes (APDs) in the EB and vacuum phototriodes in the EE. A preshower detector is placed in front of the EE, made of a Pb absorber and a high granularity active layer composed by silicon strip sensors. The shower is initiated in the Pb layer and the high granularity of the silicon layer allows to measure the shower position with high precision and to differentiate single γ photon from π^0 decays.

The figure 2.6 shows the ECAL energy resolution as a function of electron energy as measured in a beam test. The three factors entering the relation 2.2 are showed.

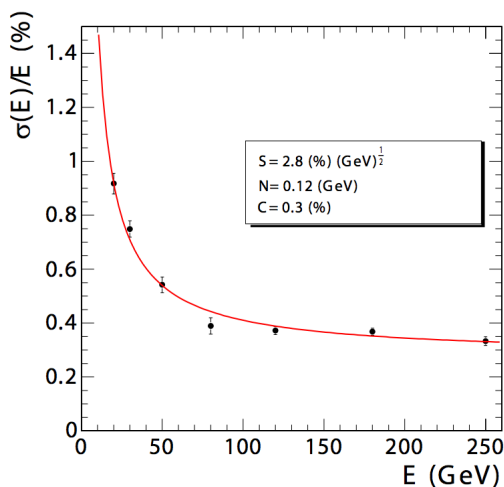


Figure 2.6 – ECAL energy resolution as a function of electron energy as measured in a beam test [43].

The Hadronic Calorimeter HCAL

From the center outwards, the detector layer surrounding the ECAL is the CMS hadronic calorimeter (HCAL). Unlike the ECAL, the HCAL is a sampling calorimeter made of alternating layers of brass (70% Cu, 30% Zn) as absorber and plastic scintillators as active material. The signal is then propagated by scintillating fibers and collected by avalanche photodiodes. The HCAL structure is arranged in six sections, the hadron barrel calorimeter (HB) closed by two endcap sections (HE) composes the inner part, surrounded by the hadron outer barrel calorimeter (HO) closed by two forward (HF) calorimeters, as illustrated in figure 2.7. It has a pseudorapidity coverage up to $|\eta| = 5.2$, hence larger than the ECAL.

One can define a hadronic absorption length λ_a , analogous to the EM radiation length X_0 . For an element of atomic number Z , $\lambda_a \gg X_0$, which is why the HCAL is thicker and placed after the ECAL from the point of view of the collision point. Indeed, otherwise the electrons and photons could not reach the ECAL, and the hadronic showers would not have a sufficient extent of material to develop in the detector.

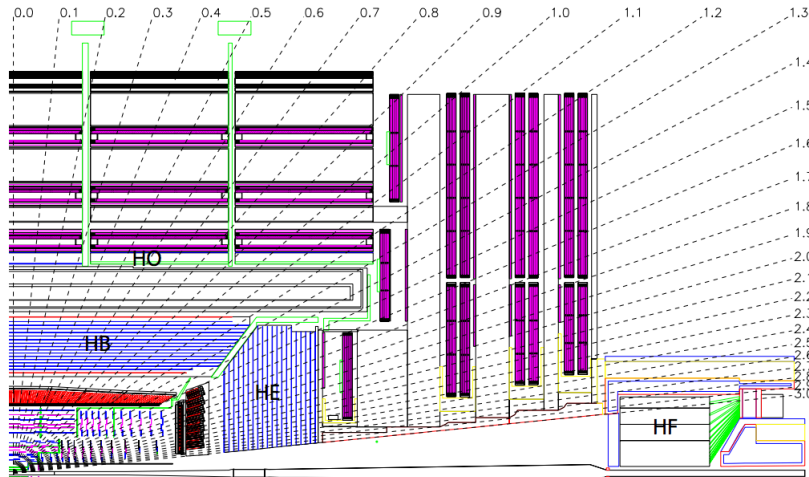


Figure 2.7 – Longitudinal view of the CMS detector showing the six composing part of the HCAL [43].

Hadronic showers are characterized by an hadronic component made essentially of π^\pm and an EM component arising from the decays of π^0 mesons into two photons. The HCAL has to be calibrated with a special design called compensation to have the same response to both components.

The transverse energy resolution for jets in the HCAL is represented in figure 2.8.

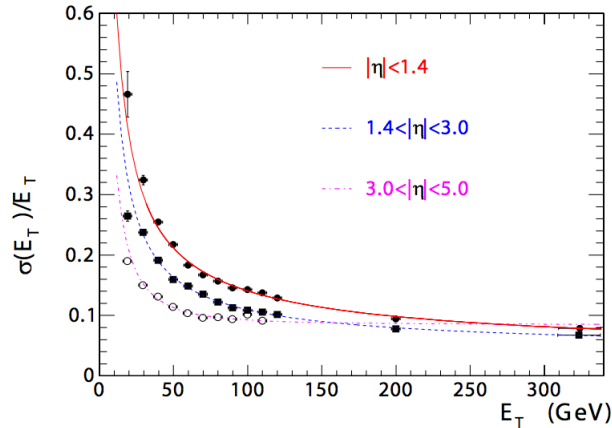


Figure 2.8 – Jet transverse energy resolution in HCAL as a function of the jet transverse-energy for different pseudorapidity regions [43].

Muon system

Processes of central interest at the LHC, such as $W/Z/H$ bosons decay or some SUSY models predicted decays come with leptonic, and in particular muonic final states, which stress out the importance of a highly performant muon detection at CMS. Muon identifi-

cation, momentum measurement and triggering are the three tasks performed by the muon system.

Muons can cross a large quantity of material without being stopped. Indeed, they do not interact strongly, hence do not undergo hard collisions corresponding to a high energy loss. They interact electromagnetically though, which mean they collide with electrons of the surrounding material, but being 200 times heavier than electrons, they do not lose much energy in this process. Finally, their large mass is also the reason why their energy loss by bremsstrahlung is negligible (at least up to energies of a few hundreds GeV) because the energy loss corresponding to this process is inversely proportional to the square of the particle mass. All those considerations characterize muons as highly penetrating particles, emphasizing the need for a special design for muon detectors.

The muon system is located around the superconducting magnet surrounding the calorimeters. The muon chambers are interleaved with three 12-sided return-yoke. The muon chambers are arranged in a barrel section closed by two endcaps and use three different types of gas detectors because of the variation of the physical conditions between the two regions.

The barrel section is made of drift tubes, consisting of stretched wires in a volume of gas contained in cylindrical tubes. When a muon crosses the drift tubes, it ionizes the gas volume. Electrons then drift to the electrodes because of the applied electric field, ending up on the positively charged wire. Multiplying the electron drift speed in the tube by the time taken for the electrons to reach the wire gives the muon original distance from the wire. The latter, combined with recorded positions of the electrons hits along the wire provide a two dimensional view of the muon position. Finally, the three layers of muon chambers in the barrel section allow a 3D reconstruction of the muon track. The barrel region has a pseudorapidity coverage of $|\eta| < 1.2$.

The two endcaps regions use cathode strip chambers (CSCs) consisting in alternating pannels of positively-charged anode wires and negatively-charged cathode strips, the space in between two pannels being filled with gas. Anode wires and cathode strips are placed orthogonally with respect to each others. CSCs are multiwire proportionnal chambers (MWPC), when a muon crosses a chamber, it ionises the gas and the drift electron creates an avalanche which induces a signal on the anode wires while positively charged ions move towards the cathode strips where they also induce a signal. The orthogonality of the electrodes allow a 2D reading for the position coordinates. CSCs provide precise time and position information and are therefore suitable for the high rate muon region that is the endcap region, and for triggering functions.

It is notable that muons cross the calorimeters without being absorbed, hence their energy is not measured. The muon system measure the muon momentum p_t but the energy-momentum relation dictates that because the scale of momentum considered in the LHC is way larger than the muon mass, energy and momentum are equal.

Finally, resistive plate chambers (RPC) form an independent muon trigger system in both barrel and endcap sections. RPC are made of two parallel-plate electrodes of high resistivity separated by a gas volume. When a crossing muon ionises the gas, the same avalanche process as described for CSCs takes place, but the high resistivity of the electrodes make them transparent to electrons, and the signal is instead read on external metallic strips. The requirements for the trigger system are to be able to simultaneously identify candidate muon

tracks, assign a bunch crossing to it and make a measure of their transverse momenta p_t . The excellent time resolution of RPC allow them to tag the time of an ionizing event in a time shorter than the timelapse between two LHC beam bunch crossings.

The combined information from the inner silicon tracker and the muon system allows cross-checking and a better resolution on the transverse momentum p_t , as shown in figure 2.9 for two regions of pseudorapidity.

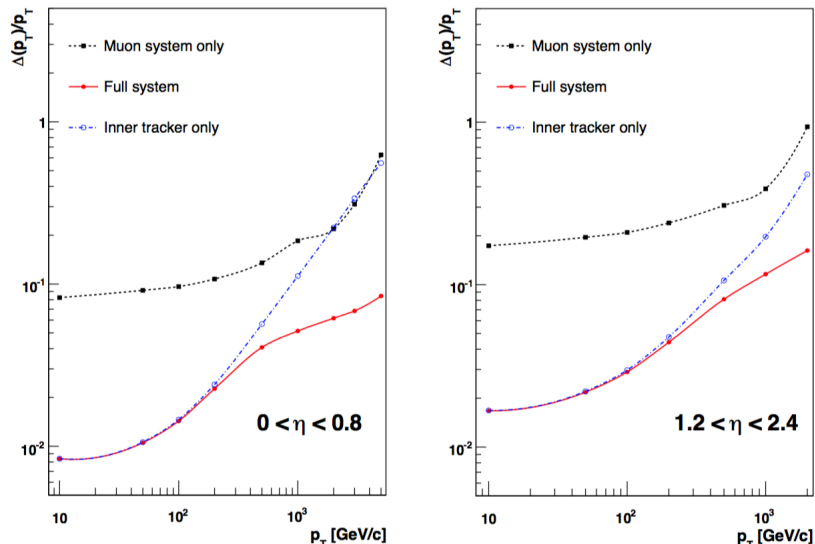


Figure 2.9 – Comparison of muon transverse momentum resolution as a function of the transverse momentum p_t using the inner tracking only, the muon system only, or both [43].

2.3.3 Trigger system

The trigger system of CMS is described in reference [20], we review hereafter the essential features of the trigger system. Inside the LHC, hundreds of million of collisions take place every second, hence it is impossible to read and store the entire related data. The CMS trigger is represented in figure 2.10. It consists in two subsystems, the level 1 (L1) trigger and the high level trigger (HLT).

The L1 uses coarsely segmented data from the calorimeters and the muon system to decide whether or not to keep an event in a timelapse of a few microseconds after a collision. During the L1 decision process, the full-resolution data is stored in the front-end pipelines. The L1 output is limited to 100 kHz meaning that the thresholds have to be adjusted during data taking in function of the value of the instantaneous luminosity. The flow of events accepted by L1 is regularized in readout buffers before being sent to a computer farm to be processed by the HLT.

The HLT is software implemented, the data processing follows a *HLT path* consisting in a set of algorithmic processing steps of growing complexity that are run in a predefined order to reconstruct the candidate object of each event selected by L1 and apply identification criteria to select events of possible interest. The HLT has an average output rate of 1000 Hz and the remaining data are stored offline for further analysis.

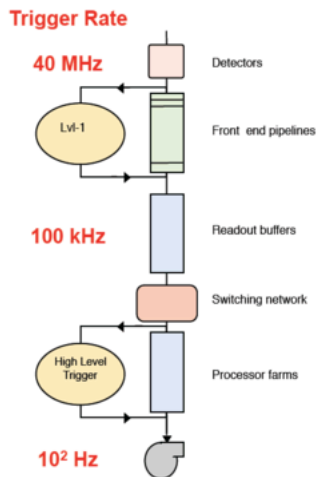


Figure 2.10 – The CMS two-levels trigger system [31].

2.4 Event reconstruction

2.4.1 Particle Flow algorithm

The CMS event reconstruction is based on the particle flow (PF) algorithm which aims at identifying and reconstructing all stable particles in a given collision, i.e. charged and neutral hadrons, muons, electrons and photons. The algorithm correlates information from different subdetectors to identify all particles from an event and then given this identification, uses the associated measurements to reconstruct the particle properties. It consists in three steps; the track reconstruction, a clustering algorithm and a link procedure [15].

The PF is well suited for the CMS detector, because the latter has a highly efficient tracking system, a large magnetic field conceding a good spatial separation between charged and neutral particle tracks and finally the large granularity of the ECAL allows to avoid overlapping.

All of the following information are taken from the reference [21], unless mentioned otherwise. The basic elements for PF are charged particle tracks, muons tracks and calorimeter clusters defined as as a group of calorimeters cells with an energy higher than a given threshold. The tracks are extrapolated from the last hit measured in the inner tracker to the calorimeters. If an extrapolated track crosses a cluster area, there are considered as *linked*. The linked elements form a *block* which is interpreted as a particle. The identification and reconstructions procedures follows a predefined order of steps; the muons candidates are first identified and reconstructed and subsequently removed from the block, then the electrons and energetic and isolated photons and finally the hadrons.

2.4.2 Muons

Muon candidates can be arranged in different categories depending on the information used to reconstruct the corresponding track. If the information used to form the track of the muon candidate comes from the muon chambers only, then it is called a *standalone muon*. One can also use a combination of the information from the inner tracker and from the muon chambers: if the projection of a standalone muon track is compatible with a track in the inner tracker, then the two tracks are matched and their hits combined and fit to form a *global muon* track. If a track in the inner tracker has a corresponding transverse momentum $p_t > 0.5 \text{ GeV}$ and total momentum $p > 2.5 \text{ GeV}$, then it is extrapolated to the muon system. If the extrapolated track from the inner tracker matches at least one track segment in the muon system, the track is called a *tracker muon* track. Then, the muon identification consists in a set of selection on the properties of the global and tracker muons, further details can be found in reference [21].

2.4.3 Electrons and isolated photons

The central feature of the electron and photon reconstruction is an energy deposit in the ECAL with little HCAL energy behind. Clusters of ECAL crystals are built around local maxima of energy and a supercluster is then formed by combining closeby clusters. A technical difficulty for reconstructing and measuring the energy of electrons and photons arises from the repeated processes of bremsstrahlung photon emission, subsequent production of e^+e^- pairs (photon conversion) in the tracker, causing a spatial diffusion of the energy around the incident direction of the primary particle. When building the supercluster, all clusters are therefore requested to be close in η but allowed to be spread in ϕ .

Electron candidates are then required to have a track geometrically matched to the supercluster. The energy loss of electrons crossing the material composing the detector is dominated by the bremsstrahlung process, of which the distribution is non gaussian. Hence, the algorithm used for the track reconstruction of electrons is not the Kalman filter but the Gaussian-sum filter, described in [9]. In addition to this ECAL based approach a complementary procedure (tracker based) has been designed to improve the reconstruction efficiency at low transverse momentum.

2.4.4 Jets

Once all muons, electrons and isolated photons have been identified and removed from the list, the remaining blocks are hadrons, that may be detected as charged or neutral hadrons and nonisolated photons. The neutral hadrons are identified from clusters in the ECAL and HCAL with no matching track in the tracker. Then the charged hadrons are grouped in jets by using the *anti- k_T* algorithm. The anti- k_T algorithm [18] defines the distance d_{ij} between two objects i and j such as particles and pseudojets and the distance d_{iB} between an object i and the beam B as follows:

$$d_{ij} = \min(k_{ti}^{2p}, k_{tj}^{2p}) \frac{\Delta y_{ij}^2 + \Delta \phi_{ij}^2}{R^2}$$

$$d_{iB} = k_{ti}^{2p}$$

where $\Delta y_{ij}^2 = (y_i - y_j)^2$, $\Delta \phi_{ij}^2 = (\phi_i - \phi_j)^2$, the power p is a integer number, R is the radius of the jet and k_{ti} , y_i and ϕ_i are the transverse momentum, rapidity and polar angle of the object i respectively. The algorithm finds the smallest of the two distances d_{ij} and d_{iB} ,

if it is d_{ij} then it combines i and j and if it is d_{iB} then i is listed as a jet and removed from the object list. Then the distances are computed again and the same procedure is applied, until there are no entities left.

2.4.5 Missing transverse energy

The concept of missing energy refers to energy that is not measured by the detector but yet is expected due to energy or momentum conservation laws. Before a collision, the protons are travelling in a direction parallel to the beam, which means that the momentum in the transverse plane xy is initially zero. Therefore, any non-zero transverse momentum p_t indicates missing energy in the transverse plane, called missing transverse energy or *met*.

In the context of the PF algorithm, the *met* vector is defined as the negative of the vectorial sum of the transverse momenta of all PF particles reconstructed in the detector and is denoted PF \cancel{E}_T , or \cancel{E}_T for brevity:

$$\vec{\cancel{E}}_T = - \sum_{i=1}^N p_{T,i} \vec{e}_i$$

Chapter 3

Data and simulations

3.1 CMS 2016 data set

This analysis uses the data recorded in 2016 in the CMS detector in dielectron, dimuon and muon-electron channels, corresponding to an energy in the center of mass of the proton-proton collision $\sqrt{s} = 13 \text{ TeV}$ and an integrated luminosity of $L = 35.9 \text{ fb}^{-1}$. The figure 3.1 shows the average number of interaction per crossing in the data recorded by the CMS detector in 2016, with a mean value at 27.

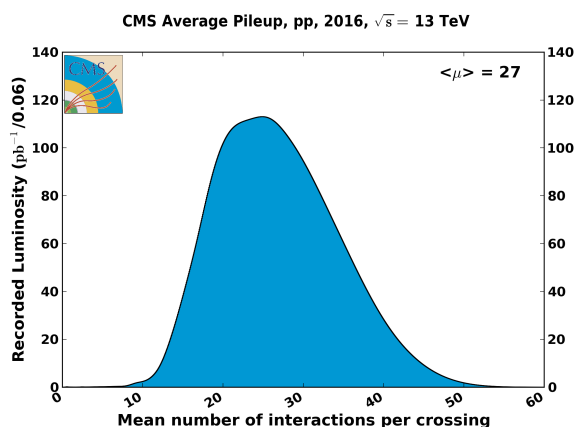


Figure 3.1 – Average pile up of the proton-proton collisions recorded in 2016 by the CMS detector [6].

3.2 Simulations

The contribution of the various processes considered in this work are estimated using simulated events, both for signal and Standard Model processes. The simulation is performed in several steps.

First the hard event, i.e. the parton-parton collision, is generated using a matrix element generator. For backgrounds, $t\bar{t}$ and diboson processes are generated with Powheg [10] while Drell-Yan, W +jets and $t\bar{t}+W/Z$ processes are generated with MadGraph5_aMC@NLO [28]. Signal events are also generated with MadGraph5_aMC@NLO.

The parton shower and hadronisation steps are then performed with the Pythia 8.219 software [41]. The parton distribution functions used are NNPDF3.0 [39] for all backgrounds

and NNPDF2.3 [38] for the signal. The generated particles are passed through a simulation of the CMS detector based on Geant 4 [30]. The samples containing the simulated events are referred to as the Monte-Carlo samples, since the generators are based on Monte-Carlo algorithms.

Finally MC samples are reconstructed with the same official CMS software used for data.

All events are generated with additional pile up collisions and reweighted to follow the exact distribution of pile up interaction observed in data as described in section 3.4.1.

The cross sections, multiplied by the branching ratios of the processes $W \rightarrow e/\mu + \nu$, corresponding to the two signal benchmarks **BMI** and **BMII** introduced in section 1.5.2 are listed in table 3.1.

The background processes considered in this work consist in processes with final states including:

- two leptons and real \cancel{E}_T : $t\bar{t}$, $t\bar{t}V$, $VV(2l2\nu)$
- two leptons and instrumental \cancel{E}_T : Drell-Yan, $VV(2l2q)$
- three leptons and real \cancel{E}_T : $WZ(3l\nu)$
- one lepton, one fake lepton and real \cancel{E}_T : $W + \text{jets}$

where $VV = ZZ/WZ/WW$ and $V = W$. All background processes are summarized in table 3.2 with their corresponding cross sections. For some of the processes, multiple samples covering different ranges of dilepton mass were used in order to increase the number of events in the region of interest. The backgrounds corresponding to QCD processes are not included, since they are expected to be negligible.

We remind here that the Drell-Yan process corresponds to the annihilation of a quark q and an antiquark \bar{q} , producing a Z boson or a virtual photon γ^* that subsequently decays into a pair of two opposite charge leptons $l\bar{l}$ of the same flavor. The quark q and antiquark \bar{q} in the initial state can radiate one or more gluons, leading to the production of jets.

Signal benchmark	Cross section [pb]
BMI	6.797e-5
BMII	1.560e-4

Table 3.1 – Cross sections of the two signal benchmarks **BMI** and **BMII** considered in this analysis, multiplied by the branching ratios of the processes $W \rightarrow e/\mu + \nu$.

Background process	Invariant mass range [GeV]	Cross section [pb]
$DY \rightarrow 2l + jets$	10-50	18610
	> 50	6020.85
	100-200	226
	200-400	7.67
	400-500	0.423
	500-700	0.24
	700-800	3.5e-2
	800-1000	3.0e-2
	1000-1500	1.6e-2
	1500-2000	2.0e-3
	2000-3000	5.4e-4
$WW \rightarrow 2l + 2\nu$	> 200	12.3
	200-600	1.386
	600-1200	5.667e-2
	1200-2500	3.557e-3
	> 2500	5.395e-5
$ZZ \rightarrow 2l + 2\nu$	/	0.564
$ZZ \rightarrow 2l + 2 quarks$	/	3.22
$WZ \rightarrow 2l + 2 quarks$	/	5.595
$WZ \rightarrow 3l + \nu$	/	4.430
$W \rightarrow jets + l + \nu$	/	61334.9
$t\bar{t} \rightarrow jets + 2l + 2\nu$	/	87.315
$t\bar{t} + W$	/	0.204
$t\bar{t} + Z$	/	0.253

Table 3.2 – List of the background processes considered in the analysis and their corresponding cross sections.

3.3 Triggers and lepton selection

Since we are interested in dilepton final states, we consider lepton pairs of opposite charge constituted of the leading lepton (denoted l_{lead}) and the trailing lepton (denoted l_{trail}) which are the leptons with highest and lowest transverse momentum p_t respectively.

The threshold values of transverse momentum p_t for electrons and muons are listed in table 3.3.

Lepton	Threshold p_t [GeV]
μ	10
e	15

Table 3.3 – Thresholds for the transverse momentum p_t for electrons and muons in this analysis.

The table 3.4 lists, for the three channels, the p_t values of the High Level Trigger of CMS and of the trigger used offline for the analysis, the latests being taken a little higher than the formers.

Lepton	Channel	HLT p_t [GeV]	Offline trigger p_t [GeV]
l_{lead}	$\mu\mu$	17	20
	$e\mu, ee$	23	25
l_{trail}	$\mu\mu, e\mu$	8	10
	ee	12	15

Table 3.4 – HLT and offline triggers for the transverse momentum p_t for the leading and trailing leptons in dimuon, dielectron and muon-electron pairs.

In order to reject jets misidentified as leptons, several conditions are applied on the reconstructed leptons. These conditions are based on various discriminating variables related for example to the quality of the muon track or to the shower shape in the calorimeters for electrons. Since one does not expect any activity around the leptons in the signal models considered, some isolation requirements are also applied. The final lepton selection follows the one used in [24].

3.4 Reweighting

It is of high importance to keep in mind that simulations only simulate physical processes hence often have flaws. The main reason is that the simulation cannot take into account each of the detector deficiencies, but also the cross sections used can be inaccurate or some processes which are calculated at leading order can have large corresponding next to leading order corrections. For all those reasons, simulated events need to be treated carefully and to be reweighted. The total weight is the square of the sum of weights w_i^2 :

$$W = \sqrt{\sum_i w_i^2}$$

Hereafter, the reweighting corrections computed and taken into account in this analysis are presented.

3.4.1 Pile-up reweighting

For each bunch crossing in the CMS detector, several proton-proton collisions take place. The term pile-up refers to all interactions not coming from the proton-proton interaction under study. The pile-up is calculated by comparison with the number of proton-proton interactions in data. Hence, the MC are reweighted according to the number of proton-proton interactions in data, and this procedure is called the pile-up reweighting.

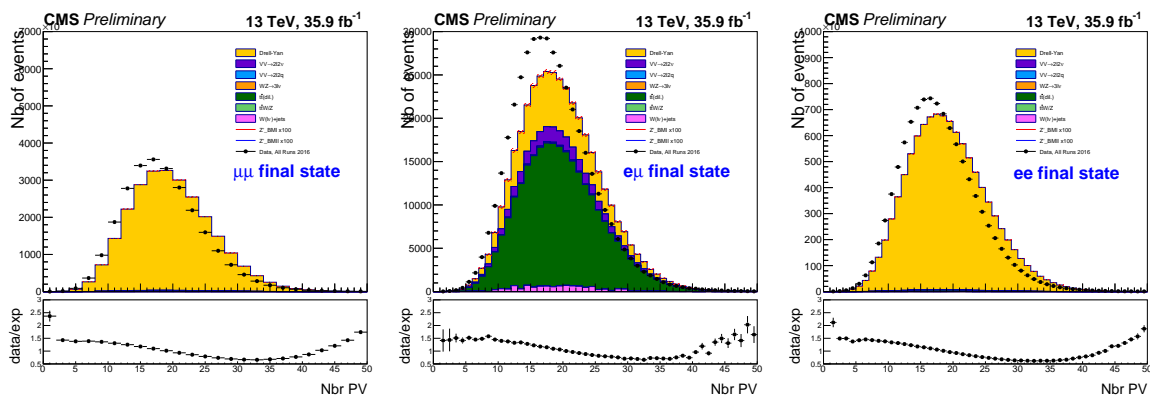


Figure 3.2 – Number of primary vertices for dimuon, electron-muon and dielectron channels after the pile-up reweighting has been performed. The number of events is in linear scale.

One can see in figure 3.2 that even after the pile-up reweighting, the MC curve is still shifted on the right with respect to data. This is a known feature, thought to come from the lower probability to reconstruct a vertex in data than in MC.

The histograms in figure 3.2 shows that the main background in dimuon and dielectron channels is due to the Drell-Yan process while in the muon-electron channel, the background is mainly arising from the process $t\bar{t} \rightarrow jets + 2l + 2\nu$. The histogram for the electron-muon channel shows a substantial amount of background due to the Drell-Yan process, which may be surprising at first considering that the Drell-Yan process requires the two leptons in the final state to be of the same flavor. This is due to $\tau\bar{\tau}$ pairs produced by the Drell-Yan process that subsequently decay into a muon and an electron via the processes:

$$\tau \rightarrow e + \bar{\nu}_e + \nu_\tau$$

$$\bar{\tau} \rightarrow \bar{\mu} + \nu_\mu + \bar{\nu}_\tau$$

or vice-versa.

3.4.2 Trigger and reconstruction renormalisation factors

In order to account for trigger and reconstruction efficiencies, MC are normalised to the Z peak by selecting two well identified leptons of the same flavor in the range in invariant

mass $60 < M_{inv} < 120 \text{ GeV}$. In practice, for dimuon and dielectron channels, it means that MC are reweighted according to a normalisation factor defined such that the number of data events on number of MC events ratio is equal to one on the Z peak region. The normalisation factor for the muon-electron channel is deduced from the ones for dielectron and dimuon channels according to:

$$\epsilon_{e\mu} = \sqrt{\epsilon_{\mu\mu} \times \epsilon_{ee}}$$

where ϵ_i denotes the renormalisation factor of a lepton in channel i . This means that we make the hypothesis that the trigger and reconstruction efficiencies can be considered for each lepton separately. The plots used for the computation of $\epsilon_{\mu\mu}$ and ϵ_{ee} are shown in figure 3.3, the factors are extracted from the *data/exp* box. The factors corresponding to the three channels are summarized in table 3.5.

The figure 3.4 shows the invariant mass M_{inv} in the three channels after the implementation of the pile-up reweighting and of the renormalization factors of table 3.5. As required by construction, the MC match well the data in dimuon and dielectron channels in the range $60 < M_{inv} < 120 \text{ GeV}$. A good match is also observed in the muon-electron channel, this validates our hypothesis to split the reconstruction and trigger efficiencies by lepton.

The excess of data with respect to MC visible in the figures 3.3 and 3.4 at small values of M_{inv} in the ee and $\mu\mu$ channels will be discussed in the next chapter.

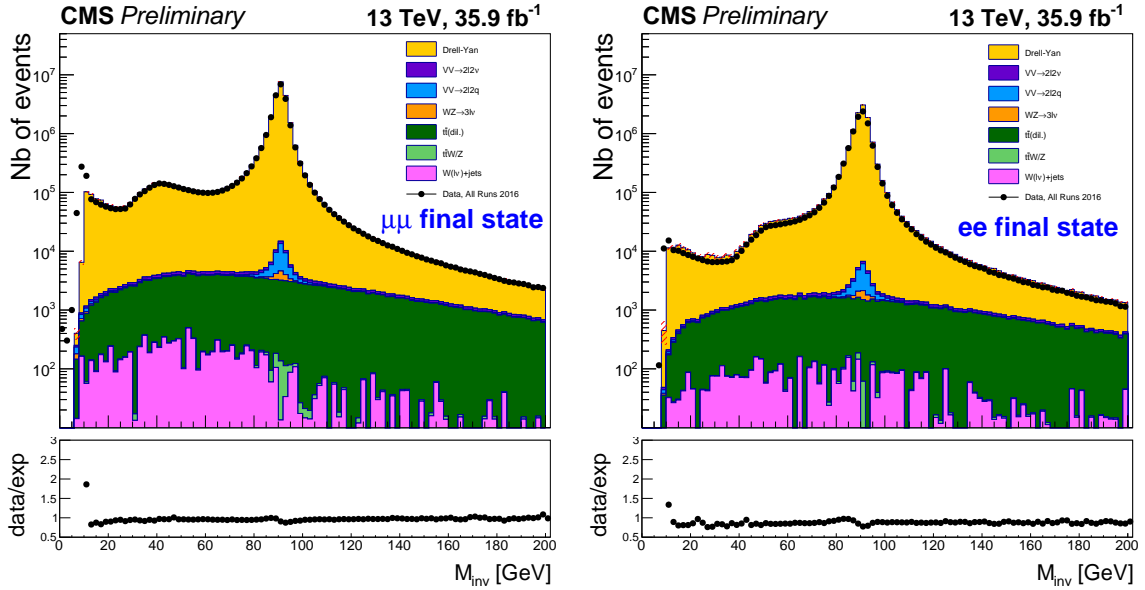


Figure 3.3 – Invariant mass in the range $0 < M_{inv} < 200 \text{ GeV}$ for dimuon and dielectron channels before reweighting.

Channel	Renormalization factor
$\mu\mu$	0.930
ee	0.847
$e\mu$	0.887

Table 3.5 – Trigger and reconstruction renormalization factors for dimuon, dielectron and muon-electron channels.

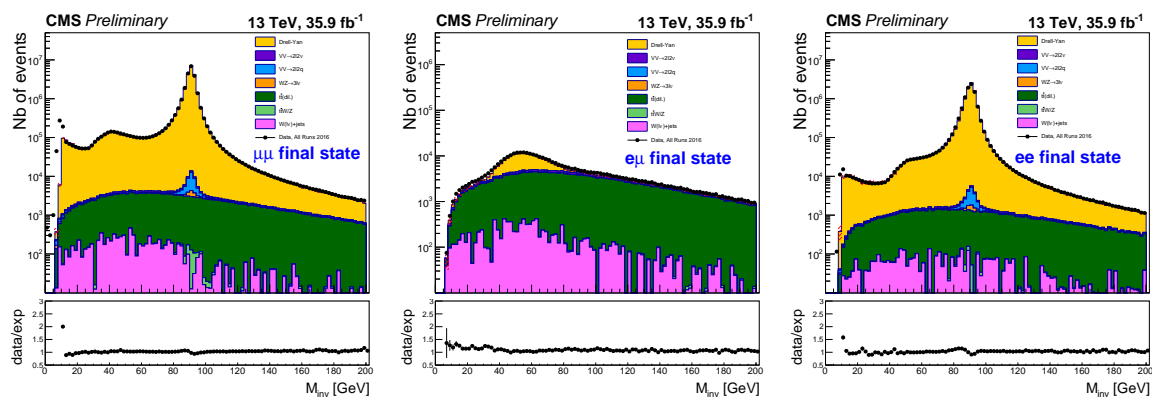


Figure 3.4 – Invariant mass in the range $0 < M_{inv} < 200 \text{ GeV}$ for dimuon, muon-electron and dielectron channels after the implementation of the pile up reweighting and the renormalization factors accounting for the trigger and reconstruction efficiencies.

Chapter 4

Implementation of the original selection from [11] and selection optimization

4.1 Implementation of the original selection from [11]

The selection of the lepton pairs as well as the threshold and trigger requirements for the leptons were presented in section 3.3.

The jets considered throughout this analysis must have transverse momenta p_t^j and pseudorapidities $|\eta^j|$ satisfying:

$$\begin{aligned} p_t^j &\geq 25 \text{ GeV} \\ |\eta^j| &< 2.4 \end{aligned}$$

Now we present the implementation of the selection proposed in table 10 of reference [11]. A few changes have been made with regard to [11] and the selection actually implemented is summarized in table 4.1. The main difference with regard to [11] is the inclusion in addition to the dimuon channel of the electron-muon and the dielectron channels in the analysis. We first review the different quantities entering the selection.

The quantity ΔR used in the step 5 of table 4.1 is defined following:

$$\Delta R = \sqrt{(\eta(l_{lead}) - \eta(l_{trail}))^2 + (\phi(l_{lead}) - \phi(l_{trail}))^2}$$

where $\eta(l_{lead}), \eta(l_{trail}), \phi(l_{lead}), \phi(l_{trail})$ are the pseudorapidity and polar angle of the leading and trailing lepton respectively.

Finally, $p_t(l_{lead}), p_t(l_{trail})$ are the transverse momentum of the leading and trailing lepton respectively and \cancel{E}_T is the missing transverse energy.

For the sake of consistency, we always present the histograms for variables entering the selection 4.1 in the following way; six plots arranged in two lines: one column for each of the three channels. On the upper line are the histograms for the variable before the step n of the selection implementing this variable, meaning all the steps up to the $n - 1$ are implemented. On the lower line are the histograms for the variable after all steps of the selection have been applied. This way of presenting illustrates the motivation for each cut of the selection.

Step	Requirement
1	$N^l = 2$
2	Electron veto (for $\mu\mu$ channel)
3	$ \eta < 1.5$
4	$\Delta R(l_{lead}, l_{trail}) > 2.5$
5	Jet Veto
6	$p_t(l_{lead}) > 300 \text{ GeV}$
7	$p_t(l_{trail}) > 200 \text{ GeV}$
8	$\cancel{E}_T > 100 \text{ GeV}$

Table 4.1 – Selection of the lepton pairs proposed in paper [11].

The legend is the same for all the histograms in this chapter but is not displayed on certain plots due to a lack of space. Black dots correspond to data while plain-colored surfaces correspond to backgrounds. It is worth noting that backgrounds are summed in the histograms, allowing to read directly the total number of events on the y-axis for a certain value of the x-axis. Red and blue lines correspond to benchmark signals **BMI** and **BMI** respectively, multiplied by a factor of a hundred for more visibility. Nevertheless, the signal is still weak and is not visible on certain plots.

The distributions of the pseudorapidity η are similar for the leading and trailing leptons, as shown in figures 4.1 and 4.2. The upper histograms show a rather flat distribution in the three channels, meaning that leading and trailing leptons are distributed uniformly in directions in the range $|\eta| < 2.4$. We may also note that the background is dominated by the Drell-Yan process for dimuon and dielectron channels and by $t\bar{t}$ in the $e\mu$ channel.

The ΔR variable is an indicator of the angular separation between the leading and the trailing lepton. We may notice two features in the upper distributions of the figure 4.3: first the excess in data with respect to MC at small ΔR in the dimuon and dielectron channels and second peak of the distribution around $\Delta R = 3$ in the three channels. The excess in data in $\mu\mu$ and ee channels is due to disintegration of Υ particles in $\mu\mu$ and ee pairs which are not taken into account by the MC. This excess is visible at small ΔR (and is therefore suppressed by the cut $\Delta R > 2.5$) because the small mass of the Υ combined with the lepton p_t thresholds induce that the leptons are not emitted back to back, hence have a small angular separation. Moreover, there is no excess visible in the $e\mu$ channel because the decay $\Upsilon \rightarrow e\mu$ is forbidden by the conservation of the lepton quantum number. The peak around $\Delta R \sim 3$ visible in the three channels correspond to Drell-Yan leptons emitted back to back, hence with $\Delta\phi = \pi$. In this situation, all particles with $|\eta| < 1$ will have $\Delta R \sim 3$ because of the quadratic nature of the terms in the definition of ΔR .

The upper histograms in figure 4.4 show a good agreement between MC and data up to seven jets for the muon-electron channel but only up to two or three jets for the dimuon and dielectron channels. This is due to the fact that, in the dimuon and dielectron channels, the main background process is Drell-Yan, meaning that jets originate from gluons emitted by the $q\bar{q}$ pair and it is a known feature that generators have trouble to describe multiple initial state radiations (ISR).

In the upper histograms in figure 4.5, we can see for dimuon and dielectron channels that the transverse momentum of the leading lepton $p_t(l_{lead})$ present a peak around $45 GeV$ and then a smooth continuous decrease for larger values. This is not surprising considering the main background is due to the Drell-Yan process. The two leptons in this process being emitted back to back, they have the same transverse momentum p_t that we can write in terms of the angle θ as follows: $p_t = p \times \sin\theta$. Hence, the leptons reach a maximum in p_t for $\theta = \frac{\pi}{2}$, when they are in the transverse plane. Then,

$$p_{t,max} = \frac{p_{max}}{2} = \frac{91 GeV}{2} \sim 45 GeV$$

where the value of p_{max} is fixed by the Z boson mass. The DY events with $p_t > 45 GeV$ can come from Z bosons that are either off-shell or boosted in the transverse plane.

The upper histograms of figure 4.6 for the transverse momentum of the trailing lepton $p_t(l_{trail})$ have a different shape with respect to the corresponding ones for the transverse momentum of the leading leptons $p_t(l_{lead})$. We observe a peak for $p_t(l_{trail}) > 300 GeV$ which comes from the fact that all the dileptons pairs produced by the Drell-Yan process having $p_t(l_{lead}) = p_t(l_{trail}) < 300 GeV$ are cut by the step 6 of the selection, $p_t(l_{lead}) > 300 GeV$.

In the lower histograms of figures 4.5 and 4.6, a substantial amount of background due to the DY process is noticeable at large value of p_t in the dimuon channel, but not in the dielectron channel. This is surprising, considering that the branching ratio of the DY process in the $\mu\mu$ and ee final states are symmetric. This feature will be discussed in section 4.2.

Finally, the figure 4.7 shows the implementation of the last step of the selection summarized in table 4.1, i.e. the cut on the missing transverse energy $\cancel{E}_T > 100 GeV$. On the upper histograms, before the cut, we see that the main background is still due to the DY process. The DY background peaks at $\cancel{E}_T = 0$, which is expected because the DY process comes with no real \cancel{E}_T in the final state. A non-zero value of the missing transverse energy for a DY event indicates a mismeasurement of the transverse momentum p_t , this will be further discussed in section 4.2.

The lower histograms shows that the cut $\cancel{E}_T > 100 GeV$ suppresses almost all DY background and the remaining background comes mainly from $t\bar{t}$ and diboson pairs VV .

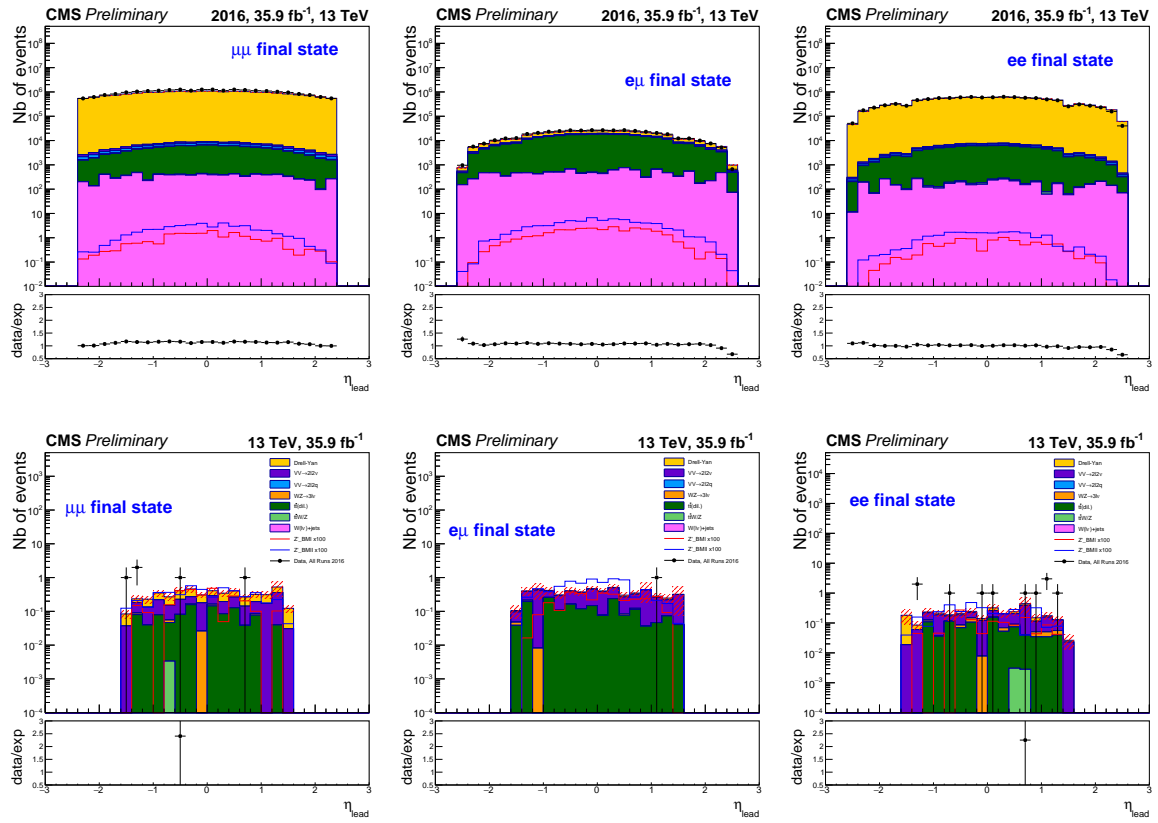


Figure 4.1 – Pseudorapidity η of the leading lepton in dimuon, electron-muon and dielectron channels, before step 3 of table 4.1 has been implemented (up) and after all steps of the selection (down).

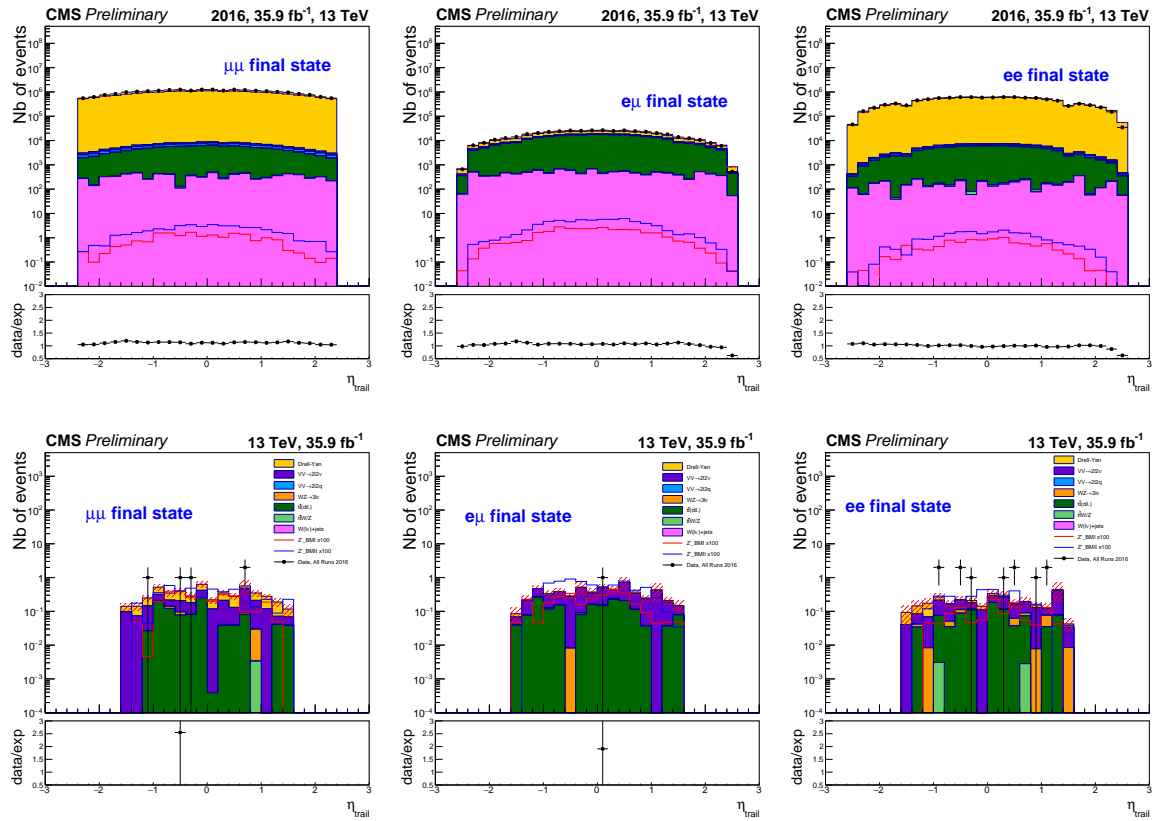


Figure 4.2 – Pseudorapidity η of the trailing lepton in dimuon, electron-muon and dielectron channels, before step 3 of table 4.1 has been implemented (up) and after all steps of the selection (down).

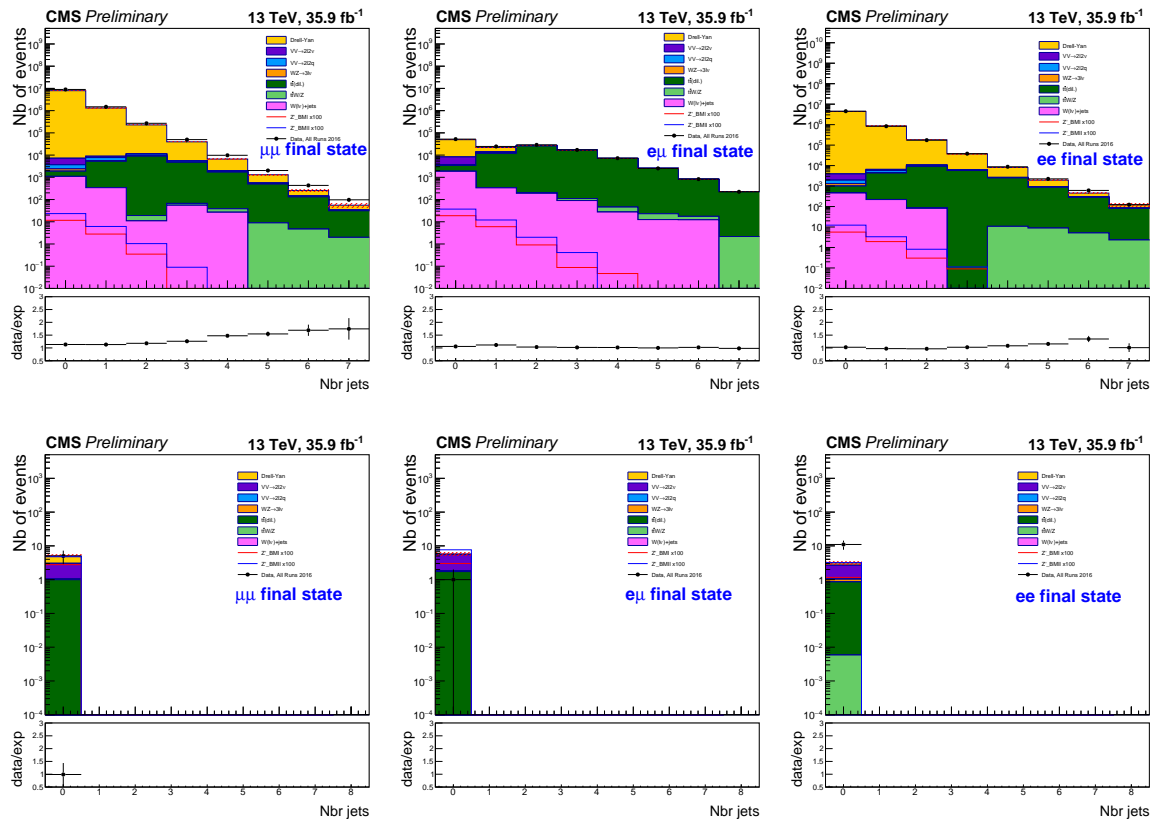


Figure 4.4 – Number of jets in dimuon, electron-muon and dielectron channels, before step 5 of table 4.1 has been implemented (up) and after all steps of the selection (down).

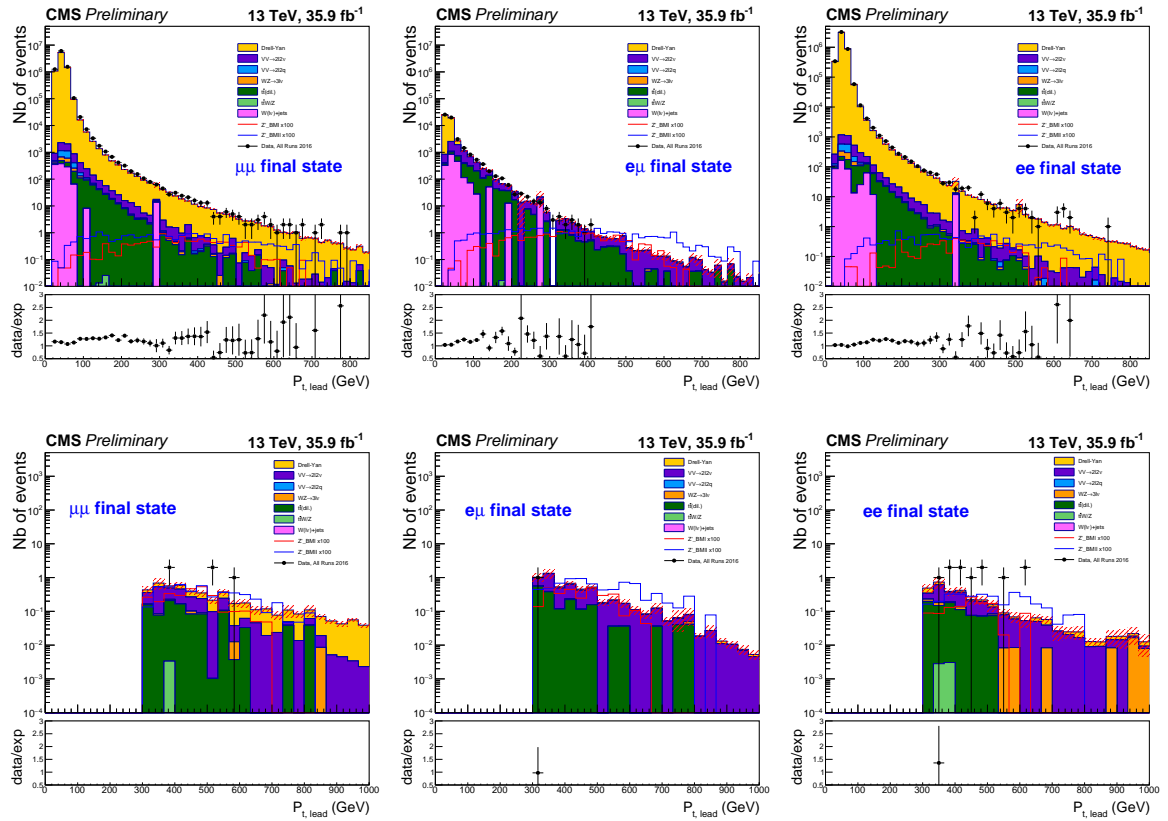


Figure 4.5 – Transverse momentum p_t of the leading lepton in dimuon, electron-muon and dielectron channels, before step 6 of table 4.1 has been implemented (up) and after all steps of the selection (down).

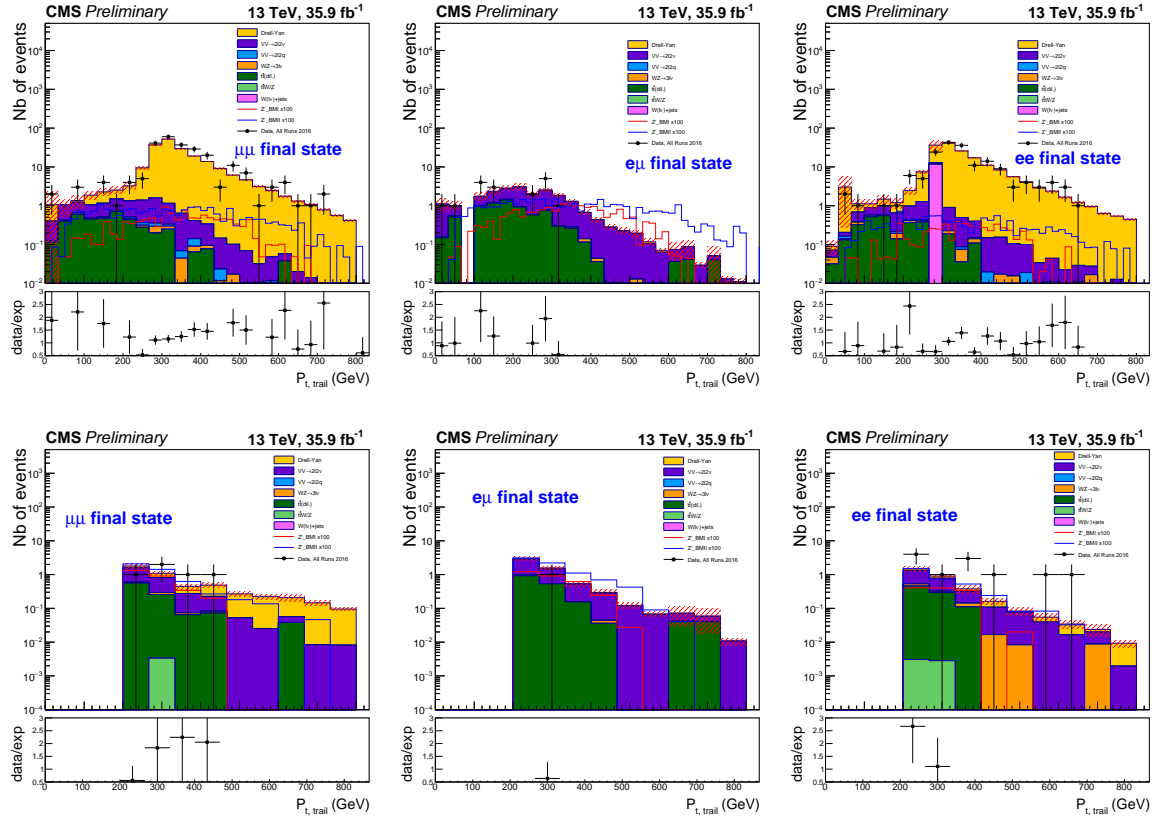


Figure 4.6 – Transverse momentum p_t of the trailing lepton in dimuon, electron-muon and dielectron channels, before step 7 of table 4.1 has been implemented (up) and after all steps of the selection (down).

4.2 Event selection optimization

In order to optimize the selection shown in table 4.1, an alternative selection, summarized in table 4.2, was designed and implemented. Following the same procedure as described in section 4.1, all variables entering the selection in table 4.2 are shown in figures 4.9 to 4.16.

Step	Requirement
1	$N^l = 2$
2	$M_{inv} > 20 \text{ GeV}$
3	$M_{inv} < 70 \text{ GeV}$ or $M_{inv} > 110 \text{ GeV}$
4	Jet Veto
5	$P_t(l_{lead}) > 200 \text{ GeV}$
6	$P_t(l_{trail}) > 100 \text{ GeV}$
7	$ \eta < 2$
8	$\cancel{E}_{met} < 100 \text{ GeV}$
9	$\cancel{E}_T > 100 \text{ GeV}$

Table 4.2 – Optimized selection

Hereafter, we review and motivate the main changes between the alternative selection 4.2 and the original selection 4.1.

The cut $\Delta R(l_{lead}, l_{trail}) > 2.5$ is replaced by two conditions on the invariant mass. In section 4.1, an excess in data with respect to MC was observed at low ΔR in dimuon and dielectron channels and assumed to be caused by the decay of Υ particles. The same excess is also visible at small values of the invariant mass in the upper histograms of figure 4.9 and is coherent with our assumption, since $m_\Upsilon = 9.46 \text{ GeV}$. Hence, we perform a cut on the small values of the invariant mass:

$$M_{inv} > 20 \text{ GeV}$$

Then in order to suppress the DY background, we set a veto on the Z peak in the $\mu\mu$ and ee channels, meaning that we restrict the invariant mass range to:

$$M_{inv} < 70 \text{ GeV} \text{ or } M_{inv} > 110 \text{ GeV}$$

In order to recover some efficiency, the cuts on the transverse momentum p_t of the leading and trailing leptons are lowered by 100 GeV each, setting the new values to:

$$p_t(l_{lead}) > 200 \text{ GeV}$$

$$p_t(l_{trail}) > 100 \text{ GeV}$$

The range in pseudorapidity has been modified to $|\eta| = 2$. This is motivated by the upper histograms in figures 4.1 and 4.2 which suggest to extend the range in pseudorapidity $|\eta|$, as it allows to recover some efficiency. The reason for extending the range up to $|\eta| = 2$ and not higher is shown in the figure 4.8: the region $2 < |\eta| < 2.4$ brings a large amount of additional background without a significant amount of additional signal in dimuon channel. This is due to high p_t muons with large η . Indeed, the resolution of the p_t declines with a growing p_t because the curvature of the track of very forward high p_t muons is difficult to measure, leading to mismeasurement of the p_t and subsequently to fake (also called instrumental) \cancel{E}_T .

Finally, we introduce a cut on a new variable, \cancel{E}_{met} which is defined as the total missing transverse energy subtracted by the missing transverse energy corresponding to the leptons. Let us first remind the reader that the missing transverse energy is define as the negative sum of the transverse momenta of all particles of a given event;

$$\vec{\cancel{E}}_T = - \sum_i \vec{P}_{t,i}$$

Since it is a vectorial quantity, it can be expressed in components;

$$\vec{\cancel{E}}_T = (met_x, met_y)$$

with

$$met_x = met \times \cos(\phi(met))$$

$$met_y = met \times \sin(\phi(met))$$

Then, the variable \cancel{E}_{met} is defined as follows:

$$\cancel{E}_{met} = \sqrt{\cancel{E}_{met_x}^2 + \cancel{E}_{met_y}^2}$$

with

$$\cancel{E}_{met_x} = met_x + p_t(l_{lead})\cos(\phi(l_{lead})) + p_t(l_{trail})\cos(\phi(l_{trail}))$$

$$\cancel{E}_{met_y} = met_y + p_t(l_{lead})\sin(\phi(l_{lead})) + p_t(l_{trail})\sin(\phi(l_{trail}))$$

The variable \cancel{E}_{met} allows to exclude events in which the \cancel{E}_T does not come (only) from the leptons, such as $t\bar{t}$ decays. The upper histograms of figure 4.15 shows the distribution of the variable \cancel{E}_{met} , we can see that the background $t\bar{t}$ has a rather flat distribution while the signal is mainly located below $\cancel{E}_{met} = 100 \text{ GeV}$. This suggest to impose the cut:

$$\cancel{E}_{met} < 100 \text{ GeV}$$

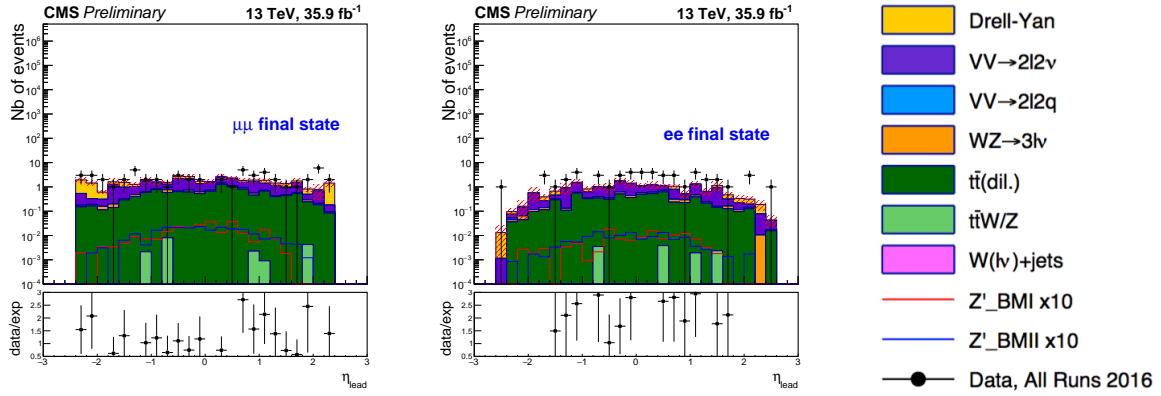


Figure 4.8 – Pseudorapidity η of the leading lepton after implementation of the selection of table 4.2 with the restriction $|\eta| < 2.4$ instead of $|\eta| < 1.5$ for dimuon and dielectron channels. Exceptionnally, the signals **BMI** and **BMII** are multiplied by a factor ten instead of a hundred.

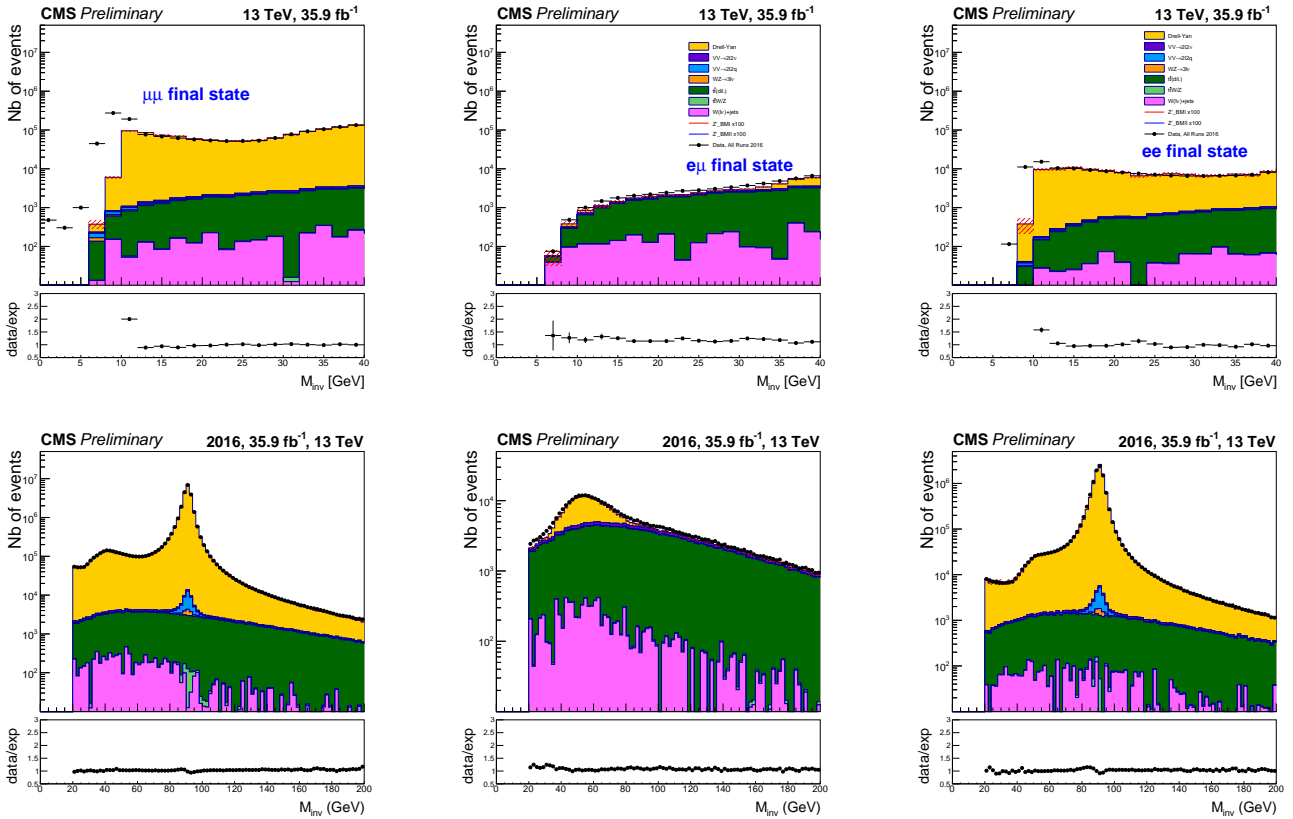


Figure 4.9 – Invariant mass M_{inv} for dimuon, muon-electron and dielectron channels before (up) and after (down) the step 2 of table 4.2, i.e. the cut $M_{inv} > 20 \text{ GeV}$. The legend is the same for all of the six plots.

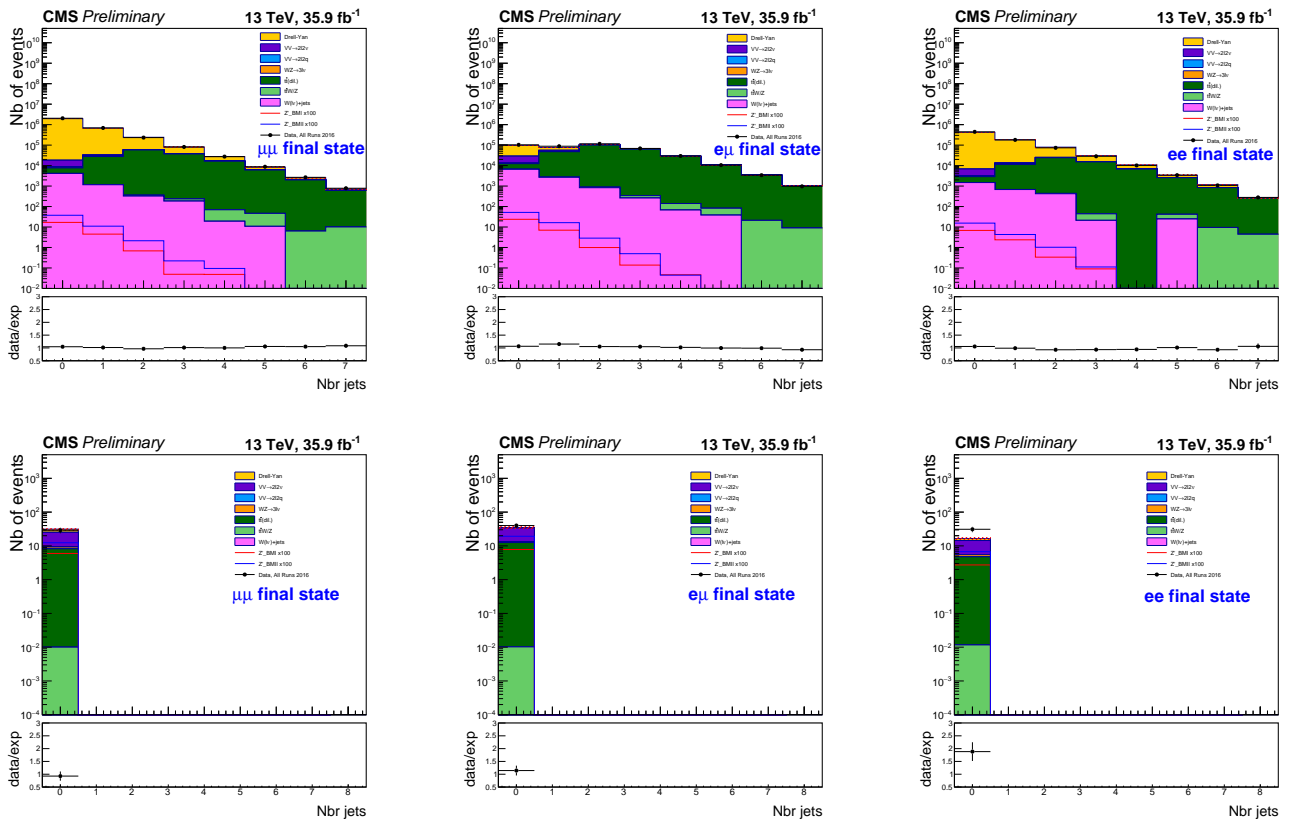


Figure 4.10 – Number of jets for dimuon, muon-electron and dielectron channels before (up) the step 4 of table 4.2 i.e. the jet veto and after all criteria have been implemented (down).

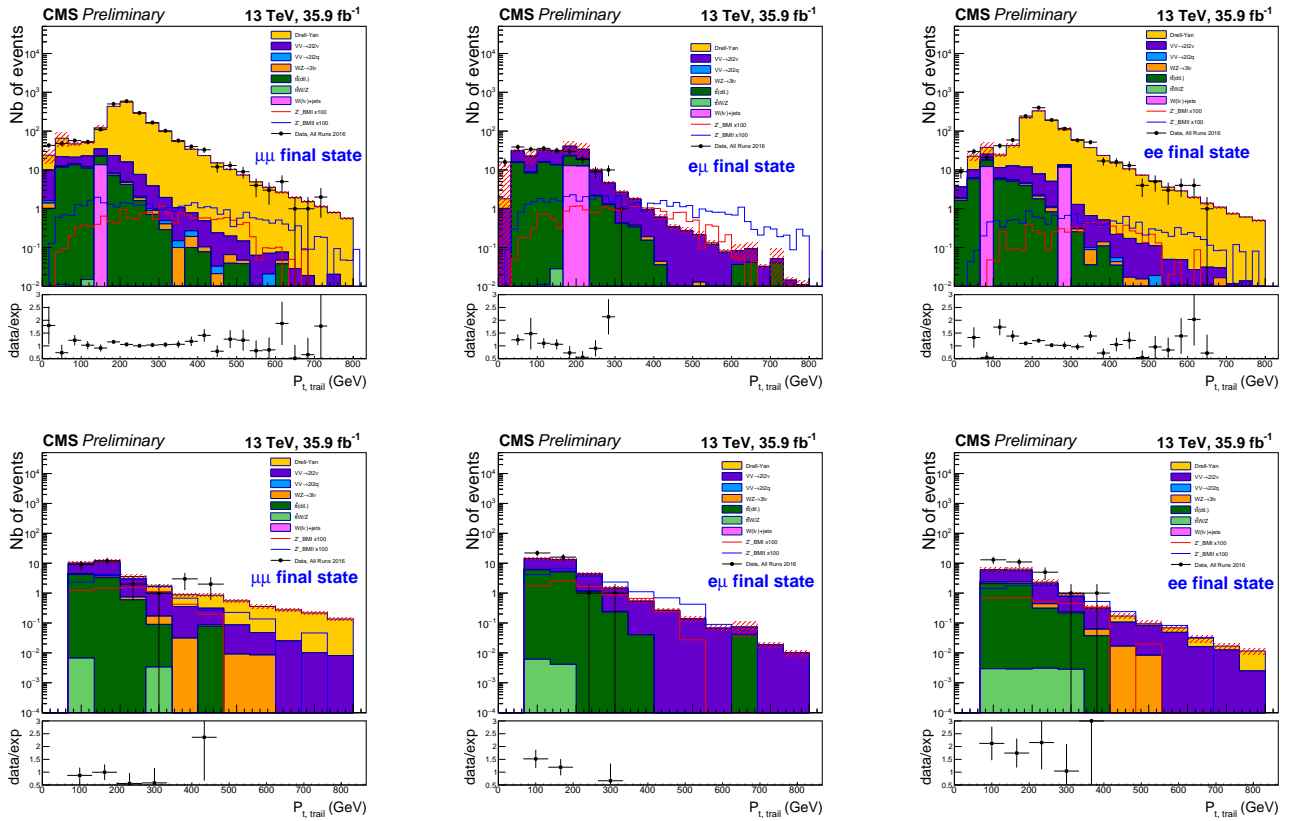


Figure 4.12 – Transverse momentum p_t of the trailing lepton for dimuon, muon-electron and dielectron channels before (up) the step 6 of table 4.2 i.e. the cut $p_t(trail) > 100 GeV$ and after all criteria have been implemented (down).

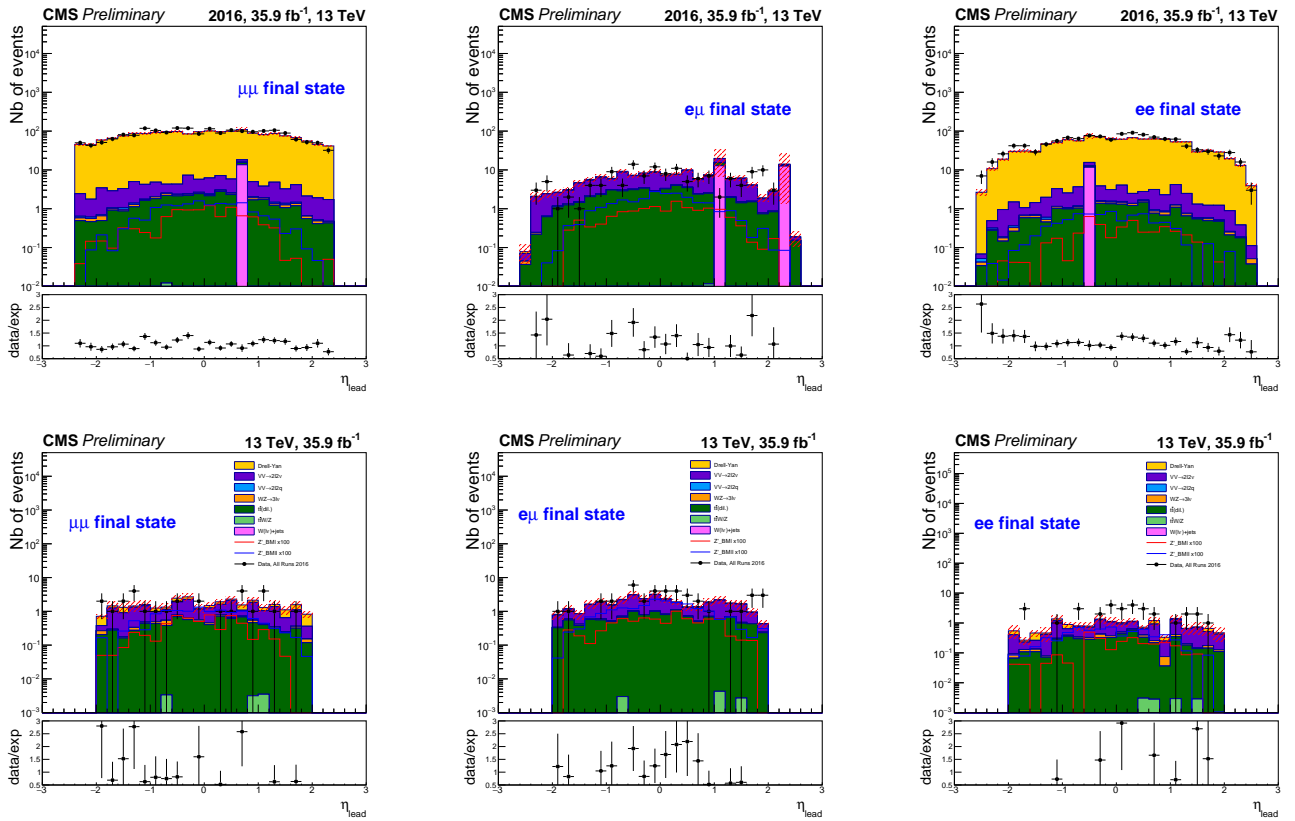


Figure 4.13 – Pseudorapidity η of the leading lepton for dimuon, muon-electron and dielectron channels before (up) the step 7 of table 4.2 i.e. the cut $|\eta| < 2$ and after all criteria have been implemented (down).

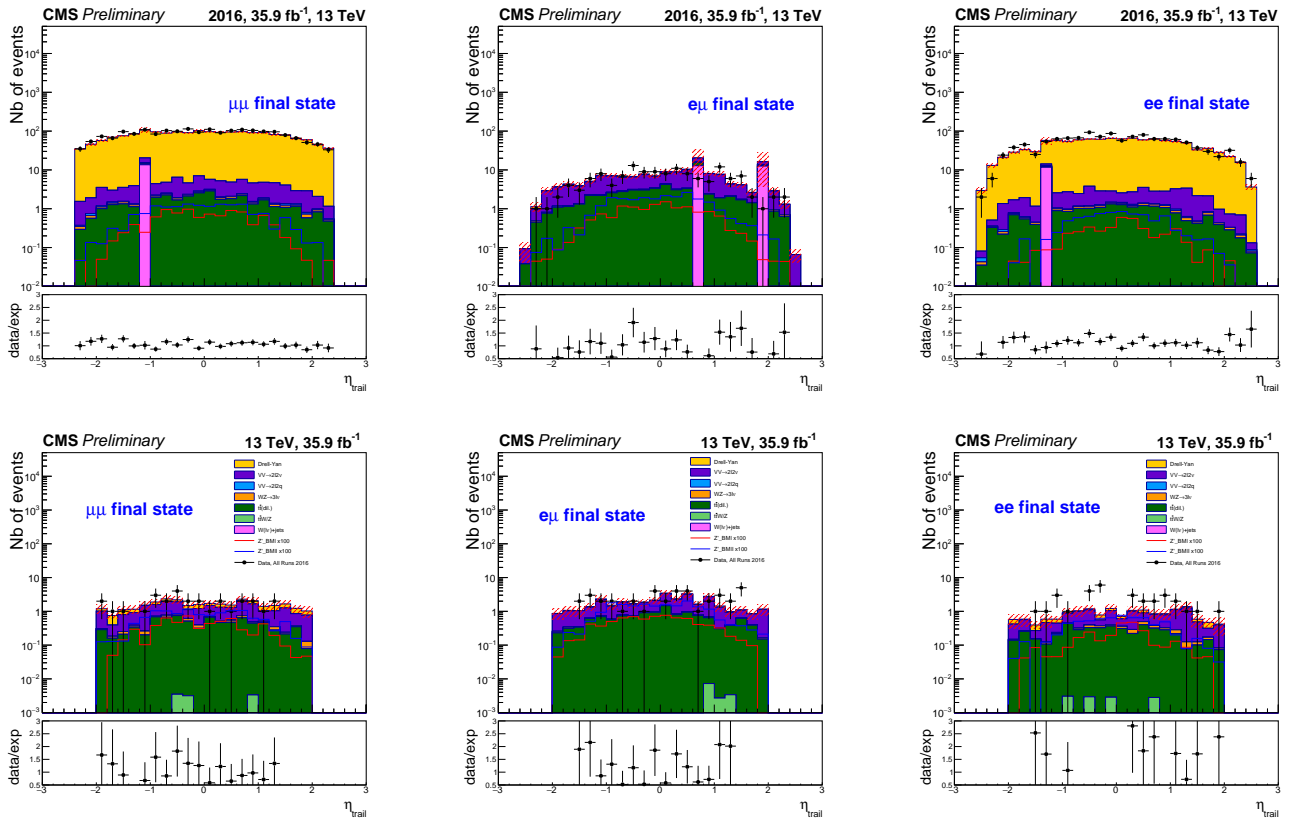


Figure 4.14 – Pseudorapidity η of the trailing lepton for dimuon, muon-electron and dielectron channels before (up) the step 7 of table 4.2 i.e. the cut $|\eta| < 2$ and after all criteria have been implemented (down).

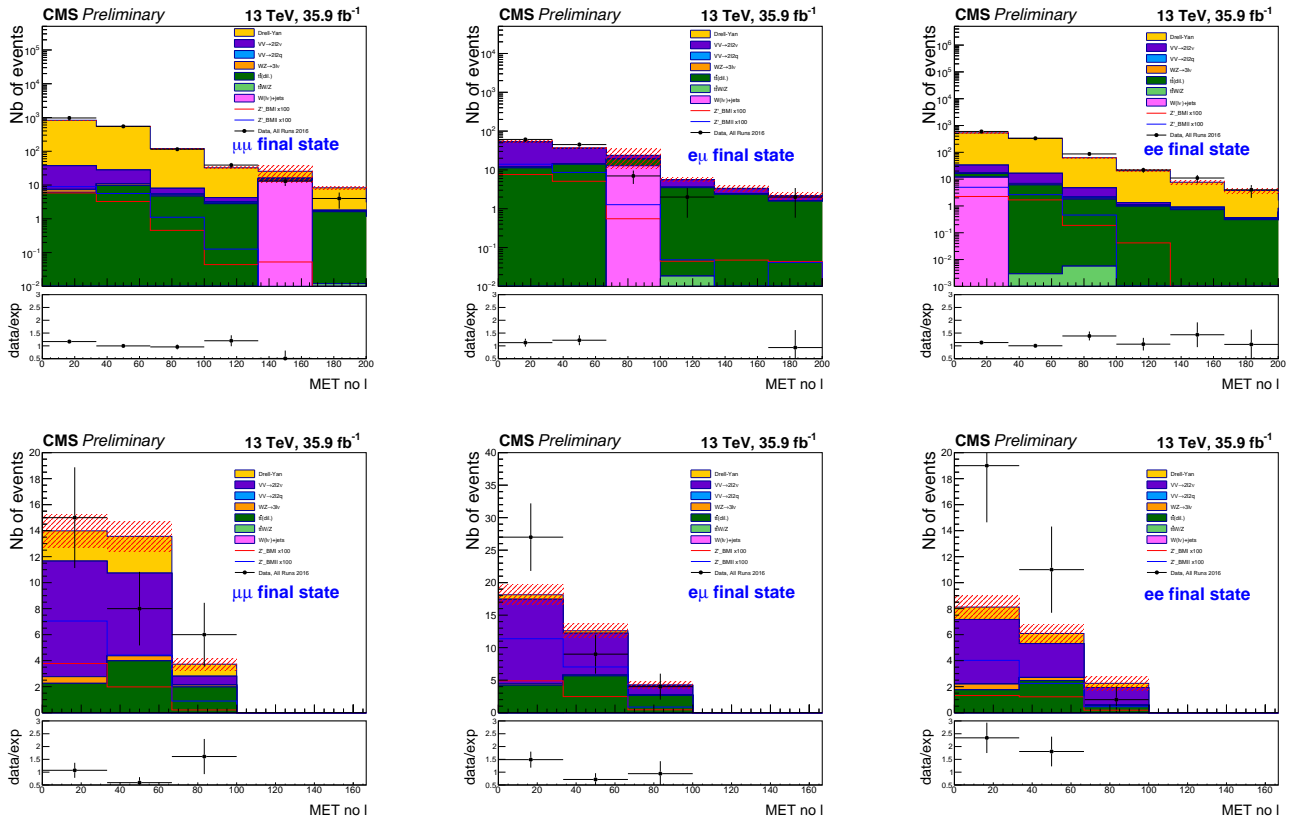


Figure 4.15 – Missing transverse energy without the leptons \cancel{L}_{met} for dimuon, muon-electron and dielectron channels before (up) the step 8 of table 4.2 i.e. the cut $\cancel{L}_{met} < 100$ GeV and after all criteria have been implemented (down).

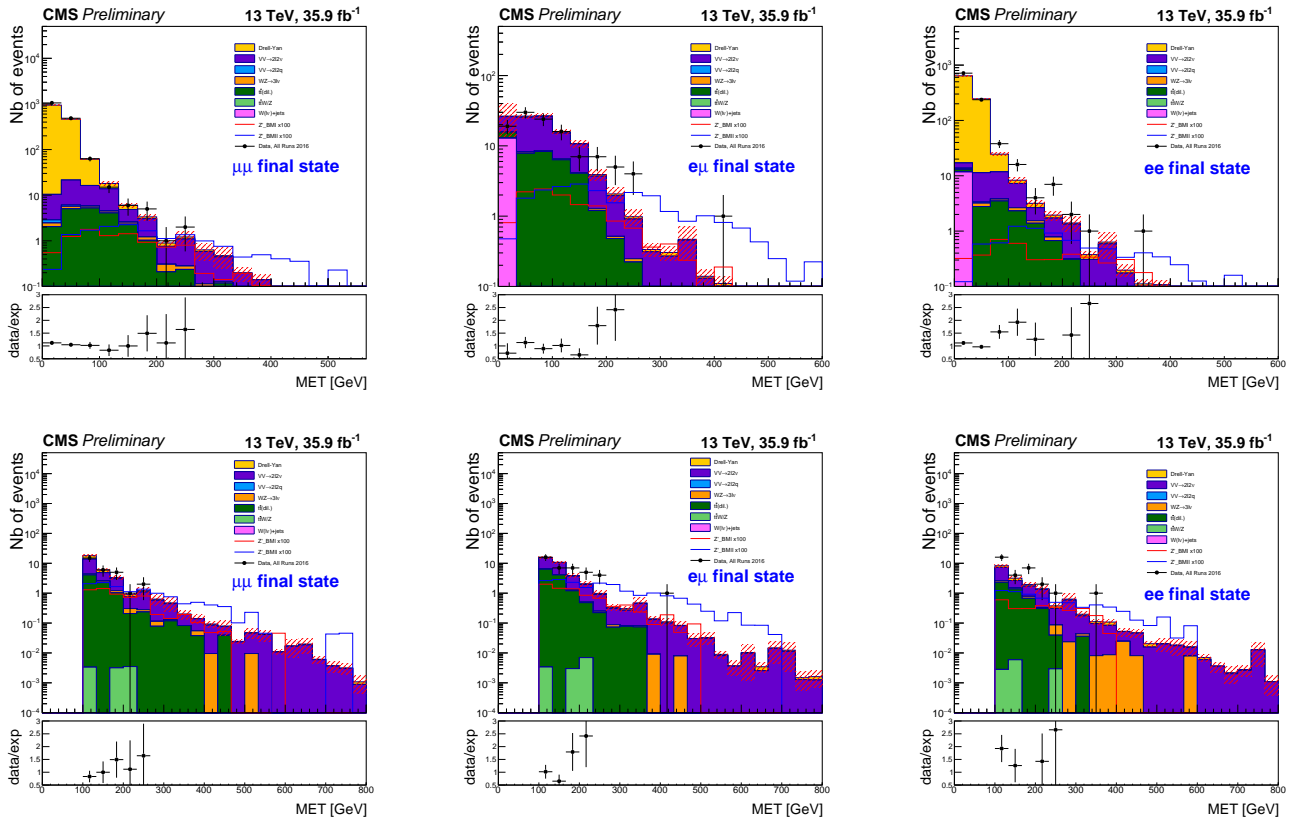


Figure 4.16 – Missing transverse energy E_T^{miss} for dimuon, muon-electron and dielectron channels before (up) and after (down) the last step of table 4.2 i.e. the cut $E_T^{\text{miss}} > 100 \text{ GeV}$.

Chapter 5

Results on the 2016 CMS data and projection for high luminosity

5.1 Results on the 2016 CMS data

The results of the implementation of the selections presented in tables 4.1 (hereafter referred to as the *original* selection) and 4.2 (hereafter referred to as the *alternative* selection) are presented for dimuon, muon-electron and dielectron channels in tables 5.1, 5.2, 5.3 and 5.4, 5.5, 5.6 respectively. The number of surviving events of backgrounds, signal (for both benchmarks **BMI** and **BMII**) and data are shown for a center of mass energy $\sqrt{s} = 13 TeV$ and an integrated luminosity $L = 35.9 fb^{-1}$.

For both selections, the data and backgrounds match well in dimuon and muon-electron channels, while a clear excess in data is visible in the dielectron channel. A possible explanation for the presence of this excess in the dielectron channel that is not seen in the dimuon channel is that jets are more often misreconstructed as electrons than as muons. In order to test our hypothesis, we need to evaluate the number of events with two jets (i.e. dijet events) misreconstructed as a dielectron event. The charges of the two jets are not correlated, hence jets are misreconstructed as dielectron pair with same sign charges with the same probability as with opposite sign charges. Therefore, we apply our selection (either the original or the alternative) with the requirement of two leptons with same sign charges instead of opposite sign charges. The result is shown for the alternative selection in figure 5.1 where we can see that only one event of data can be explained by dijet events, meaning the large data excess in dielectron channel still remains to be explained.

We define the expected significance σ as:

$$\sigma = \frac{N_{sig}}{\sqrt{N_{bg}}}$$

where N_{sig} and N_{bg} are the number of remaining event of signal (**BMI** or **BMII**) and of background respectively, after all steps of a selection have been implemented. We then define three distincts ranges of missing transverse energy \cancel{E}_T , respectively $\cancel{E}_T > 100 GeV$, $\cancel{E}_T > 200 GeV$ and $\cancel{E}_T > 300 GeV$. For each of the three channels we then evaluate the significances for **BMI** and **BMII** in each of the \cancel{E}_T ranges. Finally, for each channel, we take the maximum value of σ among the values in each \cancel{E}_T range. Our computation showed that a higher cut in \cancel{E}_T than the one considered in both selections allows to reach a larger expected significance σ . The results are shown in figure 5.2 for both the original (left) and the alternative (right) selections. The maxima of the expected significance σ are shown for each of the three channels as well as for their combination. The latter is computed as follows:

$$\sigma_{tot} = \frac{\sum_i N_{sig,i}}{\sqrt{\sum_i N_{bg,i}}}$$

for $i = \mu\mu, e\mu, ee$.

We observe immediately for both original and alternative selections that the **BMII** signal is more promising than the **BMI**, its significance being on average higher by a factor two for all channels as well as for their combination. This was expected, considering that the **BMII** has a larger production cross section than the **BMI**. The muon-electron channel represents the most interesting choice between the three channels, also for both selections, but the combination of the three channels allows a slightly higher value of σ .

Between the two selections, the alternative selection offers the highest expected significance, for both signals **BMI** and **BMII** for all channels as well as for their combination.

Step	Requirement	Background	BMI	BMII	Data
1	$N^l = 2$	2.626×10^7	0.225	0.528	2.672×10^7
2	Electron veto	2.097×10^7	0.189	0.440	2.356×10^7
3	$ \eta < 1.5$	1.106×10^7	0.149	0.338	1.279×10^7
4	$\Delta R(l_{lead}, l_{trail}) > 2.5$	9.503×10^6	0.147	0.306	1.079×10^7
5	Jet Veto	7.913×10^6	0.116	0.233	8.976×10^6
6	$P_t(l_{lead}) > 300 GeV$	207.388	0.0779	0.130	240
7	$P_t(l_{trail}) > 200 GeV$	197.305	0.0450	0.0617	230
8	$\cancel{E}_T > 100 GeV$	5.053	0.0278	0.0476	5

Table 5.1 – Results of the implementation of the original selection in the dimuon channel for a center of mass energy $\sqrt{s} = 13 TeV$ and an integrated luminosity $L = 35.9 fb^{-1}$.

Step	Requirement	Background	BMI	BMII	Data
1	$N^l = 2$	400 585	0.319	0.714	429 842
2	$ \eta < 1.5$	259 157	0.259	0.562	279 867
3	$\Delta R(l_{lead}, l_{trail}) > 2.5$	126 755	0.257	0.515	133 607
4	Jet Veto	49 406	0.187	0.371	52 283
5	$P_t(l_{lead}) > 300 \text{ GeV}$	15.361	0.117	0.213	17
6	$P_t(l_{trail}) > 200 \text{ GeV}$	13.164	0.0595	0.0928	8
7	$\cancel{E}_T > 100 \text{ GeV}$	5.789	0.0302	0.0765	1

Table 5.2 – Results of the implementation of the original selection in the muon-electron channel for a center of mass energy $\sqrt{s} = 13 \text{ TeV}$ and an integrated luminosity $L = 35.9 \text{ fb}^{-1}$.

Step	Requirement	Background	BMI	BMII	Data
1	$N^l = 2$	1.042×10^7	0.0989	0.215	1.044×10^7
3	$ \eta < 1.5$	6.492×10^6	0.0815	0.177	6.559×10^6
3	$\Delta R(l_{lead}, l_{trail}) > 2.5$	5.480×10^6	0.0797	0.166	5.594×10^6
4	Jet Veto	4.426×10^6	0.0564	0.123	4.532×10^6
5	$P_t(l_{lead}) > 300 \text{ GeV}$	179.616	0.0388	0.0697	171
6	$P_t(l_{trail}) > 200 \text{ GeV}$	171.577	0.0185	0.0363	166
7	$\cancel{E}_T > 100 \text{ GeV}$	3.177	0.0116	0.0317	11

Table 5.3 – Results of the implementation of the original selection in the dielectron channel for a center of mass energy $\sqrt{s} = 13 \text{ TeV}$ and an integrated luminosity $L = 35.9 \text{ fb}^{-1}$.

Step	Requirement	Background	BMI	BMII	Data
1	$N^l = 2$	2.626×10^7	0.225	0.528	2.672×10^7
2	$M_{inv} > 20 \text{ GeV}$	2.587×10^7	0.225	0.527	2.595×10^7
3	$M_{inv} < 70 \text{ GeV}$ or $M_{inv} > 110 \text{ GeV}$	3.009×10^6	0.221	0.509	3.094×10^6
4	Jet Veto	1.969×10^6	0.168	0.375	2.050×10^6
5	$P_t(l_{lead}) > 200 \text{ GeV}$	2018.74	0.134	0.254	2148
6	$P_t(l_{trail}) > 100 \text{ GeV}$	1882.47	0.0996	0.163	2000
7	$ \eta < 2$	1577. 28	0.0964	0.158	1700
8	$\cancel{E}_{met} < 100 \text{ GeV}$	1497.96	0.0954	0.157	1631
9	$\cancel{E}_T > 100 \text{ GeV}$	31.272	0.0597	0.124	29

Table 5.4 – Results of the implementation of the alternative selection in the dimuon channel for a center of mass energy $\sqrt{s} = 13 \text{ TeV}$ and an integrated luminosity $L = 35.9 \text{ fb}^{-1}$.

Step	Requirement	Background	BMI	BMII	Data
1	$N^l = 2$	400 585	0.319	0.714	429 842
2	$M_{inv} > 20 \text{ GeV}$	393 086	0.319	0.714	420 794
3	Jet Veto	97 117. 8	0.238	0.517	103 402
4	$P_t(l_{lead}) > 200 \text{ GeV}$	217.008	0.1878	0.366	226
5	$P_t(l_{trail}) > 100 \text{ GeV}$	160.666	0.138	0.246	137
6	$ \eta < 2$	132. 3	0.134	0.240	120
7	$\cancel{E}_{met} < 100 \text{ GeV}$	114.826	0.132	0.239	113
8	$\cancel{E}_T > 100 \text{ GeV}$	34.986	0.0780	0.192	40

Table 5.5 – Results of the implementation of the alternative selection in the muon-electron channel for a center of mass energy $\sqrt{s} = 13 \text{ TeV}$ and an integrated luminosity $L = 35.9 \text{ fb}^{-1}$.

Step	Requirement	Background	BMI	BMII	Data
1	$N^l = 2$	1.042×10^7	0.0989	0.215	1.044×10^7
2	$M_{inv} > 20 \text{ GeV}$	1.037×10^7	0.0989	0.215	1.037×10^7
3	$M_{inv} < 70 \text{ GeV}$ or $M_{inv} > 110 \text{ GeV}$	729 017	0.0961	0.209	742 811
4	Jet Veto	421 421	0.0682	0.155	445 517
5	$P_t(l_{lead}) > 200 \text{ GeV}$	1147	0.0579	0.115	1292
6	$P_t(l_{trail}) > 100 \text{ GeV}$	1098.66	0.0425	0.0822	1232
7	$ \eta < 2$	963.753	0.0416	0.0805	1068
8	$\cancel{E}_{met} < 100 \text{ GeV}$	927.198	0.0412	0.0805	1021
9	$\cancel{E}_T > 100 \text{ GeV}$	16.462	0.0272	0.0673	31

Table 5.6 – Results of the implementation of the alternative selection in the dielectron channel for a center of mass energy $\sqrt{s} = 13 \text{ TeV}$ and an integrated luminosity $L = 35.9 \text{ fb}^{-1}$.

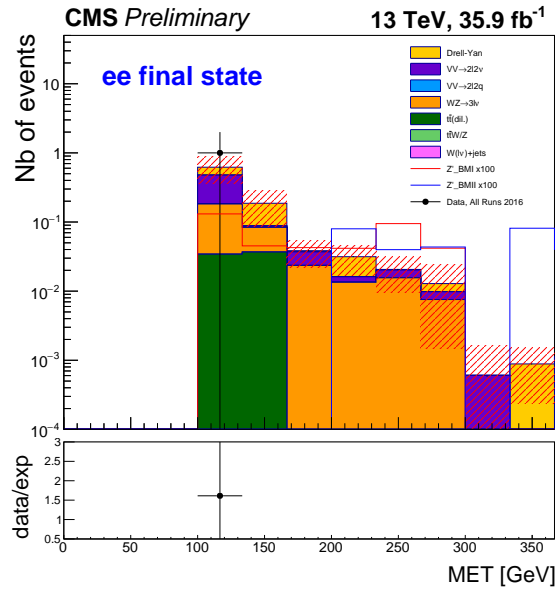


Figure 5.1 – Missing Transverse energy \cancel{E}_T for dielectron channel with the requirement of two electrons of same sign charges, after all steps of the alternative selection (table 4.2) have been implemented.

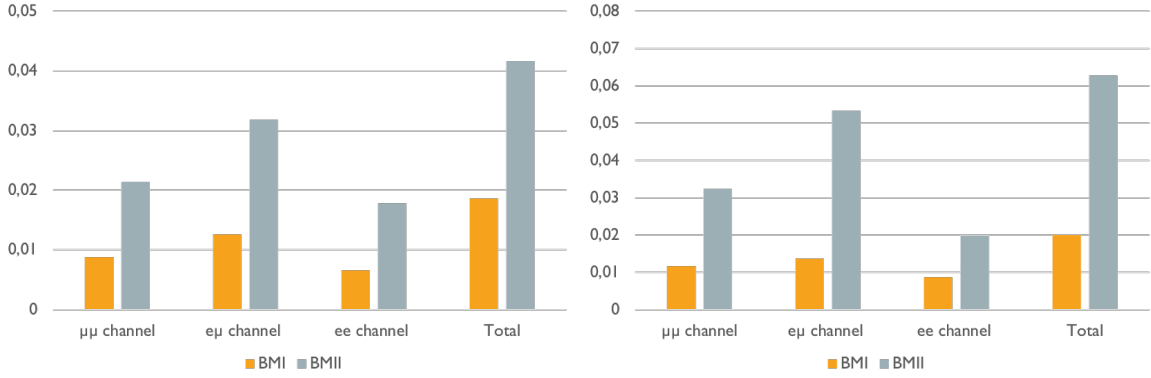


Figure 5.2 – Maximum of the expected significance σ for dimuon, muon-electron and dielectron channel, and for their combination, on the left for the original selection presented in table 4.1 and on the right for the alternative selection presented in table 4.2. The results correspond to $\sqrt{s} = 13 TeV$ and $L = 35.9 fb^{-1}$.

5.2 Projection for high luminosity

We present here the projection at the integrated luminosity $L = 3000 fb^{-1}$ of the results of the original and alternative selections (listed in tables 4.1 and 4.2 respectively). This is done by scaling the number of remaining events after the selections to the luminosity $L = 3000 fb^{-1}$ and by computing again the maximum of σ following the same procedure as in section 5.1. Following the pattern of section 5.1, the figure 5.3 shows the maxima of the expected significance σ for both **BMI** and **BMII** signals in each of the three decay channels and for their combination.

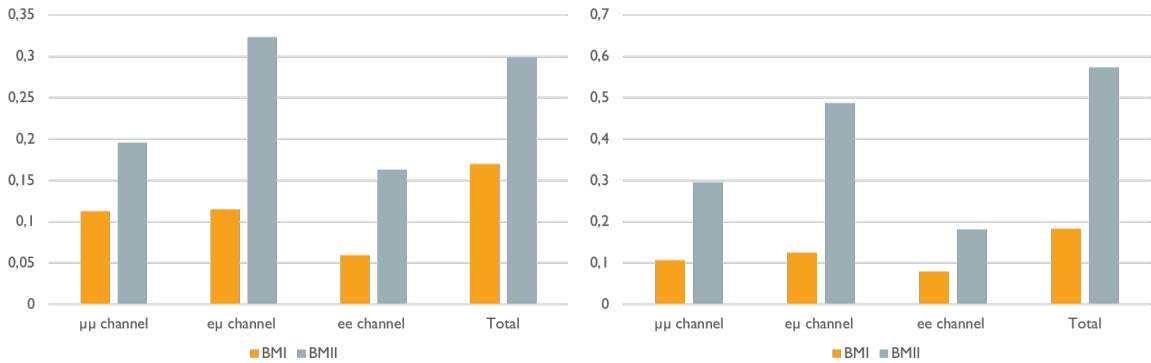


Figure 5.3 – Maximum of the expected significance σ for dimuon, muon-electron and dielectron channel, and for their combination, on the left for the original selection presented in table 4.1 and on the right for the alternative selection 4.2. The results correspond to $\sqrt{s} = 13 TeV$ and $L = 3000 fb^{-1}$.

The expected significances σ are on average higher by a factor ten with respect to the ones computed for an integrated luminosity $L = 35.9 fb^{-1}$ but still remain too small to confirm or infirm the model presented in section 1.5.2.

The results presented in this section correspond to an energy in the center of mass of the

collision $\sqrt{s} = 13 \text{ TeV}$ while the results of paper [11] correspond to $\sqrt{s} = 14 \text{ TeV}$. The ratio of the production cross section for **BMI** and **BMI** corresponding to the two values of \sqrt{s} is ~ 1.2 ¹:

$$\frac{\sigma(14 \text{ TeV})}{\sigma(13 \text{ TeV})} \sim 1.2$$

Therefore, even by accounting for the difference between the production cross sections, our results show much more background events and less signal events than expected by the reference [11]. This leads to the expected significance σ being smaller than the ones announced by the reference [11].

1. This information comes from a discussion with the authors of paper [11].

Conclusions and prospects

In the context of searches for physics beyond the Standard Model with CMS, we studied the sensitivity reach of the detector to a new physics model featuring Grand Unification Theories and Supersymmetry [11]. This model considers a scenario where a new heavy gauge boson (Z') coupling to supersymmetric particles has a significant production cross section at the LHC and that could be observed in the dilepton + missing transverse energy final state.

In this work, an analysis using the $L = 35.9 \text{ fb}^{-1}$ of data recorded in the dilepton channel at CMS in 2016 at $\sqrt{s} = 13 \text{ TeV}$ is carried out. We also present projections for an integrated luminosity $L = 3000 \text{ fb}^{-1}$ corresponding to the full data set accumulated by the end of High-Luminosity LHC run.

After presenting the theoretical aspects of the considered model and the experimental set up in the first and second chapter respectively, the analyzed data set and the simulated samples used to describe the relevant SM backgrounds are introduced in the third chapter. In order to account for the different selection efficiencies, we derive correction factors in data and simulations by using dilepton events in the Z peak mass region.

The fourth chapter describes the implementation of a selection for the lepton pairs similar to the one proposed in the paper [11], with the main difference that we extend the analysis to the $e\mu$ and ee channels in addition to the $\mu\mu$ channel. The resulting distributions of the variables entering the selection showed possibilities to improve the selection. Hence we designed and implemented an alternative selection, with reduced thresholds on the lepton transverse momentum p_T and a additional cut on the missing transverse energy without the leptons \cancel{E}_{met} . The results showed a good agreement between data and Monte-Carlo in the dimuon and muon-electron channels, but an excess was observed in data in the dielectron channel. As an attempt to explain this excess, we inverted the opposite charge condition on the two leptons in order to look for a possible contribution of processes with jets misidentified as leptons. The presence of only one such event rules out a significant contribution of these processes. Hence, to this day, this excess remains to be understood.

We then computed the expected significance σ for different ranges in missing transverse energy \cancel{E}_T for both **BMI** and **BMII** signals for each of the three channels and then consistently selected the highest value of σ among the values of each range of \cancel{E}_T . We then computed the expected significance for their combination. Our computation shows that a higher cut in \cancel{E}_T allows to reach higher σ . The results corresponding to an integrated luminosity $L = 35.9 \text{ fb}^{-1}$, confirmed that the alternative selection is more effective to isolate the signal than the original selection. For both cases, the second benchmark **BMII** is always the most promising, which was expected considering its has a larger production cross section than **BMI**. Between the three channels, the electron-muon $e\mu$ provides the highest expected significance but the combination of the three channels allows to reach the best results. Nevertheless the order of magnitude of the values of the significance σ are small, with a maximum $\sigma = 0.04$ for the combination of the three channels for the second bench-

mark **BMII**. This came as no surprise knowing that the paper [11] considered an integrated luminosity $L = 3000 \text{ fb}^{-1}$.

Finally we performed a projection of the expected significance σ to the integrated luminosity $L = 3000 \text{ fb}^{-1}$ considered in the paper [11]. This was done by scaling the number of events to the luminosity $L = 3000 \text{ fb}^{-1}$ and computing again the maximum of σ following the same procedure as before. The results showed values of the expected significance σ on average ten times larger than the results for an integrated luminosity $L = 35.9 \text{ fb}^{-1}$. Therefore, with a maximum value $\sigma \sim 0.6$, the expected significance is still too small in order to confirm or infirm the model. Our results show an expected significance smaller than the one announced by the reference [11], even by accounting for the difference between the production cross sections at 13 TeV and 14 TeV .

In conclusion, we have shown that lowering the cuts on the p_T of leading and trailing leptons in combination with an increase of the cut on the missing transverse energy \cancel{E}_T with respect to the original selection proposed in [11] improves the significance σ , eventhough it remains too small to draw conclusions about the veracity of the model, even at $L = 3000 \text{ fb}^{-1}$.

The perspective of improvements for this analysis are multiple. The reason of the different conclusions with respect to [11] regarding the CMS sensitivity to the model considered would need to be understood (much larger backgrounds and lower signal efficiency in our implementation of the selection than in [11]). Moreover, the excess of dielectron events in data would need to be investigated. Another important step would be the quantification in terms of significance and excluded cross sections of the agreement between 2016 data and predictions. Ultimately, the analysis should be carried out on the full data set recorded by CMS at $\sqrt{s} = 13 \text{ TeV}$ between 2016 and 2018. The results could also be interpreted for other choices of parameters in the model described in [11] (e.g. for a different Z' mass). Further improvements of the analysis can also be considered such as a multibin approach for signal extraction (based on \cancel{E}_T and possibly other variables) or a retuning of the lepton selection criteria.

List of Figures

1.1	Particle content of the Standard Model of particle physics [8].	6
1.2	Running of the gauge couplings for $SU(3)_C$ (in green), $SU(2)_L$ (in red) and $U(1)_Y$ (in blue) as a function of energy without (left) and with (right) the MSSM included in the theory [26].	8
1.3	Schematic representation of the production of a dilepton and missing energy final state originating from the W mediated decay of a chargino pair itself induced by a Z' boson [11].	10
2.1	CERN accelerators complex [4].	14
2.2	Integrated luminosity as function of time over a one year period, for each of the LHC running year [6].	16
2.3	Representation of the CMS detector [3].	17
2.4	Coordinate system of the CMS detector [7].	17
2.5	View of the CMS tracker in the r-z plane [42].	19
2.6	ECAL energy resolution as a function of electron energy as measured in a beam test [43].	20
2.7	Longitudinal view of the CMS detector showing the six composing part of the HCAL [43].	21
2.8	Jet transverse energy resolution in HCAL as a function of the jet transverse-energy for different pseudorapidity regions [43].	21
2.9	Comparison of muon transverse momentum resolution as a function of the transverse momentum p_t using the inner tracking only, the muon system only, or both [43].	23
2.10	The CMS two-levels trigger system [31].	24
3.1	Average pile up of the proton-proton collisions recorded in 2016 by the CMS detector [6].	27
3.2	Number of primary vertices for dimuon, electron-muon and dielectron channels after the pile-up reweighting has been performed. The number of events is in linear scale.	31
3.3	Invariant mass in the range $0 < M_{inv} < 200 GeV$ for dimuon and dielectron channels before reweighting.	32
3.4	Invariant mass in the range $0 < M_{inv} < 200 GeV$ for dimuon, muon-electron and dielectron channels after the implementation of the pile up reweighting and the renormalization factors accounting for the trigger and reconstruction efficiencies.	33
4.1	Pseudorapidity η of the leading lepton in dimuon, electron-muon and dielectron channels, before step 3 of table 4.1 has been implemented (up) and after all steps of the selection (down).	37

4.2	Pseudorapidity η of the trailing lepton in dimuon, electron-muon and dielectron channels, before step 3 of table 4.1 has been implemented (up) and after all steps of the selection (down).	38
4.3	ΔR between the leading and the trailing leptons in dimuon, electron-muon and dielectron channels, before step 4 of table 4.1 has been implemented (up) and after all steps of the selection (down).	39
4.4	Number of jets in dimuon, electron-muon and dielectron channels, before step 5 of table 4.1 has been implemented (up) and after all steps of the selection (down).	40
4.5	Transverse momentum p_t of the leading lepton in dimuon, electron-muon and dielectron channels, before step 6 of table 4.1 has been implemented (up) and after all steps of the selection (down).	41
4.6	Transverse momentum p_t of the trailing lepton in dimuon, electron-muon and dielectron channels, before step 7 of table 4.1 has been implemented (up) and after all steps of the selection (down).	42
4.7	Missing transverse energy \cancel{E}_T in dimuon, electron-muon and dielectron channels, before step 8 of table 4.1 has been implemented (up) and after all steps of the selection (down).	43
4.8	Pseudorapidity η of the leading lepton after implementation of the selection of table 4.2 with the restriction $ \eta < 2.4$ instead of $ \eta < 1.5$ for dimuon and dielectron channels. Exceptionnally, the signals BMI and BMII are multiplied by a factor ten instead of a hundred.	46
4.9	Invariant mass M_{inv} for dimuon, muon-electron and dielectron channels before (up) and after (down) the step 2 of table 4.2, i.e. the cut $M_{inv} > 20 GeV$. The legend is the same for all of the six plots.	46
4.10	Number of jets for dimuon, muon-electron and dielectron channels before (up) the step 4 of table 4.2 i.e. the jet veto and after all criteria have been implemented (down).	47
4.11	Transverse momentum p_t of the leading lepton for dimuon, muon-electron and dielectron channels before (up) the step 5 of table 4.2 i.e. the cut $p_t(lead) > 200 GeV$ and after all criteria have been implemented (down).	48
4.12	Transverse momentum p_t of the trailing lepton for dimuon, muon-electron and dielectron channels before (up) the step 6 of table 4.2 i.e. the cut $p_t(trail) > 100 GeV$ and after all criteria have been implemented (down).	49
4.13	Pseudorapidity η of the leading lepton for dimuon, muon-electron and dielectron channels before (up) the step 7 of table 4.2 i.e. the cut $ \eta < 2$ and after all criteria have been implemented (down).	50
4.14	Pseudorapidity η of the trailing lepton for dimuon, muon-electron and dielectron channels before (up) the step 7 of table 4.2 i.e. the cut $ \eta < 2$ and after all criteria have been implemented (down).	51
4.15	Missing transverse energy without the leptons \cancel{E}_{met} for dimuon, muon-electron and dielectron channels before (up) the step 8 of table 4.2 i.e. the cut $\cancel{E}_{met} < 100 GeV$ and after all criteria have been implemented (down).	52
4.16	Missing transverse energy \cancel{E}_T for dimuon, muon-electron and dielectron channels before (up) and after (down) the last step of table 4.2 i.e. the cut $\cancel{E}_T > 100 GeV$	53
5.1	Missing Transverse energy \cancel{E}_T for dielectron channel with the requirement of two electrons of same sign charges, after all steps of the alternative selection (table 4.2) have been implemented.	58

5.2	Maximum of the expected significance σ for dimuon, muon-electron and dielectron channel, and for their combination, on the left for the original selection presented in table 4.1 and on the right for the alternative selection presented in table 4.2. The results correspond to $\sqrt{s} = 13 \text{ TeV}$ and $L = 35.9 \text{ fb}^{-1}$	59
5.3	Maximum of the expected significance σ for dimuon, muon-electron and dielectron channel, and for their combination, on the left for the original selection presented in table 4.1 and on the right for the alternative selection 4.2. The results correspond to $\sqrt{s} = 13 \text{ TeV}$ and $L = 3000 \text{ fb}^{-1}$	59

List of Tables

1.1	Denomination of the bosonic supersymmetric partners of SM fermions.	7
1.2	Denomination of the fermionic supersymmetric partners of the SM bosons. . .	7
1.3	Parameters for the reference points of the two signal benchmarks BMI and BMII , taken from [11].	10
1.4	Selection of paper [11] for an energy in the center of mass of the collision $\sqrt{s} = 14 TeV$ and an integrated luminosity $L = 3000 fb^{-1}$	12
3.1	Cross sections of the two signal benchmarks BMI and BMII considered in this analysis, multiplied by the branching ratios of the processes $W \rightarrow e/\mu + \nu$	28
3.2	List of the background processes considered in the analysis and their corresponding cross sections.	29
3.3	Thresholds for the transverse momentum p_t for electrons and muons in this analysis.	30
3.4	HLT and offline triggers for the transverse momentum p_t for the leading and trailing leptons in dimuon, dielectron and muon-electron pairs.	30
3.5	Trigger and reconstruction renormalization factors for dimuon, dielectron and muon-electron channels.	33
4.1	Selection of the lepton pairs proposed in paper [11].	35
4.2	Optimized selection	44
5.1	Results of the implementation of the original selection in the dimuon channel for a center of mass energy $\sqrt{s} = 13 TeV$ and an integrated luminosity $L = 35.9 fb^{-1}$	55
5.2	Results of the implementation of the original selection in the muon-electron channel for a center of mass energy $\sqrt{s} = 13 TeV$ and an integrated luminosity $L = 35.9 fb^{-1}$	56
5.3	Results of the implementation of the original selection in the dielectron channel for a center of mass energy $\sqrt{s} = 13 TeV$ and an integrated luminosity $L = 35.9 fb^{-1}$	56
5.4	Results of the implementation of the alternative selection in the dimuon channel for a center of mass energy $\sqrt{s} = 13 TeV$ and an integrated luminosity $L = 35.9 fb^{-1}$	57
5.5	Results of the implementation of the alternative selection in the muon-electron channel for a center of mass energy $\sqrt{s} = 13 TeV$ and an integrated luminosity $L = 35.9 fb^{-1}$	57
5.6	Results of the implementation of the alternative selection in the dielectron channel for a center of mass energy $\sqrt{s} = 13 TeV$ and an integrated luminosity $L = 35.9 fb^{-1}$	58

Bibliography

- [1] http://inspirehep.net/record/1294662/files/Figures_T_Coordinate.png.
- [2] <https://cmsexperiment.web.cern.ch/sites/cmsexperiment.web.cern.ch/files/howcmsworks.png>.
- [3] <https://commons.wikimedia.org/wiki/File:Cern-accelerator-complex.svg>.
- [4] <https://root.cern.ch/>.
- [5] <https://twiki.cern.ch/twiki/bin/view/CMSPublic/LumiPublicResults>.
- [6] https://wiki.physik.uzh.ch/cms/latex:example_spherical_coordinates.
- [7] <http://www.physik.uzh.ch/groups/serra/StandardModel.html>.
- [8] ADAM, W., FRÜHWIRTH, R., STRANDLIE, A., AND TODOR, T. Reconstruction of Electrons with the Gaussian-Sum Filter in the CMS Tracker at the LHC. [<http://inspirehep.net/record/876045?ln=fr>].
- [9] ALIOLI, S., NASON, P., OLEARI, C., AND RE, E. A general framework for implementing NLO calculations in shower Monte Carlo programs: the POWHEG BOX. *Journal of High Energy Physics*, 6 (2010). [<https://arxiv.org/abs/1002.2581>].
- [10] ARAZ, J. Y., CORCELLA, G., FRANK, M., AND FUKS, B. Loopholes in Z' searches at the LHC: exploring supersymmetric and leptophobic scenarios. *Journal of High Energy Physics* 2 (2018), 92. [<https://arxiv.org/abs/1711.06302>].
- [11] ATLAS COLLABORATION. Search for new high-mass phenomena in the dilepton final state using 36 fb^{-1} of proton-proton collision data at $\sqrt{s} = 13 \text{ TeV}$ with the ATLAS detector. *Journal of High Energy Physics* 10 (2017), P. 182. [<https://arxiv.org/abs/1707.02424>].
- [12] ATLAS COLLABORATION. Search for new phenomena in dijet events using 37 fb^{-1} of pp collision data collected at $\sqrt{s} = 13 \text{ TeV}$ with the ATLAS detector. *Phys. Rev. D* 96, 5 (03 2017). [<https://arxiv.org/pdf/1703.09127>].
- [13] BAER, H., AND TATA, X. *Weak scale supersymmetry: from superfields to scattering events*. Cambridge University Press, 03 2012.
- [14] BEAUDETTE, F. The CMS Particle Flow Algorithm. *Proceedings of the CHEF2013 Conference* (01 2014). [<https://arxiv.org/abs/1401.8155>].
- [15] BURGESS, C., AND MOORE, G. *The standard model: A primer*. Cambridge University Press, 2006.
- [16] CACCIARI, M., SALAM, G. P., AND SOYEZ, G. The anti-kt jet clustering algorithm. *Journal of High Energy Physics*, 04 (2008), p. 063. [<https://arxiv.org/abs/0802.1189>].
- [17] CMS COLLABORATION. Missing transverse energy performance of the CMS detector. *Journal of Instrumentation* 6, 09 (2011), p. 09001. [<https://arxiv.org/abs/1106.5048>].

- [18] CMS COLLABORATION. The CMS trigger system. *Journal of Instrumentation* 12, 01 (09 2017), p. 01020. [<https://arxiv.org/abs/1609.02366>].
- [19] CMS COLLABORATION. Particle-flow reconstruction and global event description with the cms detector. *JINST* 12, 10 (2017), p. 10003. [<https://arxiv.org/abs/1706.04965>].
- [20] CMS COLLABORATION. Search for dijet resonances in proton-proton collisions at $\sqrt{s} = 13$ TeV and constraints on dark matter and other models. *Phys. Lett. B* 769 (11 2017), pp. 520–542. [<https://arxiv.org/abs/1611.03568>].
- [21] CMS COLLABORATION. Search for high mass resonances in dielectron final state. [<http://inspirehep.net/record/1662534/?ln=fr>].
- [22] CMS COLLABORATION, SIRUNYAN, A., AND TUMASYAN, A. E. A. Search for supersymmetry in events with at least three electrons or muons, jets, and missing transverse momentum in proton-proton collisions at $\sqrt{s} = 13$ TeV. *J. High Energy Phys.* 67 (2018). [[https://doi.org/10.1007/JHEP02\(2018\)067](https://doi.org/10.1007/JHEP02(2018)067)].
- [23] CORCELLA, G. Phenomenology of supersymmetric Z' decays at the Large Hadron Collider. *Eur. Phys. J. C* 75, 6 (12 2015), 264. [<https://arxiv.org/abs/1412.6831>].
- [24] DELLA VECCHIA, R. *Moduli spaces of gauge theories in 3 dimensions*. PhD thesis, Università degli studi di Padova, 2015.
- [25] DOUGHTY, N. *Lagrangian interaction: an introduction to relativistic symmetry in electrodynamics and gravitation*. CRC Press, 1990.
- [26] ET AL., J. A. The automated computation of tree-level and next-to-leading order differential cross sections, and their matching to parton shower simulations. *Journal of High Energy Physics* 07 (2014).
- [27] FABJAN, C. W. Calorimetry for particle physics. *Reviews of Modern Physics* 75, 4 (2003), pp. 1243–1286.
- [28] GEANT4 COLLABORATION. GEANT4—a simulation toolkit. *Nuclear instruments and methods in physics research section A: Accelerators, Spectrometers, Detectors and Associated Equipment* 506, 3 (2003), pp.250–303.
- [29] HALYO, V., HUNT, A., JINDAL, P., LEGRESLEY, P., AND LUJAN, P. GPU enhancement of the trigger to extend physics reach at the LHC. *Journal of Instrumentation* 8, 10 (2013), p. 10005. [<https://arxiv.org/abs/1305.4855>].
- [30] KRIPPENDORF, S., QUEVEDO, F., AND SCHLOTTERER, O. Cambridge Lectures on Supersymmetry and Extra Dimensions. [<https://arxiv.org/abs/1011.1491>].
- [31] LANGACKER, P. The physics of heavy Z gauge bosons. *Reviews of Modern Physics* 81, 3 (2009), p. 1199. [<https://arxiv.org/abs/0801.1345>].
- [32] LEIKE, A. The phenomenology of extra neutral gauge bosons. *Physics Reports* 317, 3-4 (1999), pp. 143–250. [<https://arxiv.org/abs/hep-ph/9805494>].
- [33] LYKKEN, J. D. Beyond the Standard Model. *CERN Yellow Report CERN-2010-002* (05 2010), pp. 101–109. [<https://arxiv.org/abs/1005.1676>].
- [34] MARTIN, S. P. A Supersymmetry Primer. [<https://arxiv.org/abs/hep-ph/9709356>].
- [35] MIRMAN, N., WANG, Y., AND ALEXANDER, J. Missing transverse energy significance at CMS. *Proceedings, 2nd Conference on Large Hadron Collider Physics Conference* (06 2014). [<https://arxiv.org/abs/1409.3028>].
- [36] NNPDF COLLABORATION. Parton distributions with LHC data. *Nuclear Physics B* 867, 2 (2013), pp. 244–289. [<https://arxiv.org/abs/1207.1303>].

- [37] NNPDF COLLABORATION. Parton distributions for the LHC Run II. *Journal of High Energy Physics* 04 (2015), p. 40. [<https://arxiv.org/abs/1410.8849>].
- [38] SARKAR, U. LEP constraints on Grand Unified Theories. *Pramana* 41, 1 (1993), pp. 261–269.
- [39] SJÖSTRAND, T., MRENNNA, S., AND SKANDS, P. A brief introduction to PYTHIA 8.1. *Computer Physics Communications* 178, 11 (2008), pp. 852–867. [<https://arxiv.org/abs/0710.3820>].
- [40] VILIANI, L. CMS tracker performance and readiness for LHC run II. *Nuclear Instruments and Methods in Physics Research Section A: Accelerators, Spectrometers, Detectors and Associated Equipment* 824 (2016), pp. 67–69.
- [41] VOSS, R., AND BRESKIN, A., Eds. *The CERN Large Hadron Collider, accelerator and experiments*, vol. 2. 2009.
- [42] WEINZIERL, S. Introduction to Monte Carlo methods. *Topical lectures given at the Research School Subatomic Physics, Amsterdam* (06 2000). [<https://arxiv.org/abs/hep-ph/0006269>].
- [43] WONG, C.-Y. *Introduction to high-energy heavy-ion collisions*. World Scientific, 1994.